

1           **Effects of three-dimensional electric field on saltation during dust**  
2                           **storms: An observational and numerical study**

3

4   Huan Zhang<sup>1</sup>, You-He Zhou<sup>1,\*</sup>

5

6           <sup>1</sup>Department of Mechanics and Engineering Science, College of Civil Engineering and  
7                   Mechanics, Lanzhou University, Key Laboratory of Mechanics on Disaster and  
8           Environment in Western China, The Ministry of Education of China, Lanzhou 730000,  
9   PR China.

10

11           \*Correspondence to: You-He Zhou ([zhouyh@lzu.edu.cn](mailto:zhouyh@lzu.edu.cn))

12

1 **Abstract.** Particle triboelectric charging being ubiquitous in nature and industry,  
2 potentially plays a key role in dust events, including the lifting and transport of sand  
3 and dust particles. However, the properties of the electric field (E-field) and its  
4 influences on saltation during dust storms remain obscure as the high complexity of  
5 dust storms and the existing numerical studies mainly limited to one-dimensional (1-  
6 D) E-field. Here, we quantify the effects of real three-dimensional (3-D) E-field on  
7 saltation [during dust storms](#), through a combination of field observations and  
8 numerical modelling. The 3-D E-fields in the sub-meter layer from 0.05 to 0.7 m above  
9 the ground during a dust storm are measured at Qingtu Lake Observation Array site.  
10 The time-varying mean of E-field series [over a certain timescale](#) are extracted by the  
11 discrete wavelet transform and ensemble empirical mode decomposition methods.  
12 The measured results show that each component of the 3-D E-field data roughly  
13 collapses on a single 3-order polynomial curve when normalized. Such 3-D E-field data  
14 close to the ground within a few centimeters has never been reported and formulated  
15 before. Using discrete element method, we then develop a comprehensive saltation  
16 model, in which the triboelectric charging between particle-particle midair collisions  
17 is explicitly accounted for, allowing us to evaluate the triboelectric charging in saltation  
18 [during dust storms](#) properly. By combining the results of measurements and modelling,  
19 we find that although the vertical component of the E-field (i.e. 1-D E-field) inhibits  
20 sand transport, 3-D E-field enhances sand transport substantially. Furthermore, the  
21 model predicts that 3-D E-field enhances the total mass flux and saltation height by up  
22 to 20 % and 15 %, respectively. This suggests that a 3-D E-field consideration is  
23 necessary if one is to explain precisely how the E-field affects saltation during dust  
24 storms. These results further improve our understanding of particle triboelectric  
25 charging in saltation and help to provide more accurate characterizations of sand and  
26 dust transport during dust storms.

27  
28  
29

## 1 **1. Introduction**

2 Contact or triboelectric charging is ubiquitous in dust events (Harrison et al., 2016;  
3 Kok and Renno, 2008; Lacks and Sankaran, 2011; Schmidt et al., 1998; Zheng et al.,  
4 2003). The pioneering electric field (E-field) measurements in dust storms by W. A.  
5 Douglas Rudge showed that the vertical atmospheric E-field was substantially  
6 increased to 5-10 kV m<sup>-1</sup> and **its direction reversed** (became upward-pointing) during  
7 a severe dust storm (Rudge, 1913). Later measurements in dust storms found  
8 downward-pointing (Esposito et al., 2016), upward-pointing (Bo and Zheng, 2013; Yair  
9 et al., 2016; Zhang and Zheng, 2018), and even alternating vertical E-field which  
10 continually reverses direction (Kamra, 1972; Williams et al., 2009), with the magnitude  
11 of up to ~100 kV m<sup>-1</sup>.

12 The significant influences of E-field on **pure saltation (that is, in the absence of**  
13 **suspended dust/aerosol particles)** have been verified, both numerically (e.g. Kok and  
14 Renno, 2008; Zhang et al., 2014) and experimentally (e.g. Esposito et al., 2016;  
15 Rasmussen et al., 2009). The effects of E-field on saltation **during dust storms**, however,  
16 remain obscure. A clear **difference** between the numerical simulation and field  
17 measurement is that: numerical simulation **of pure saltation** showed a reduction in  
18 saltation mass flux by E-field (e.g. Kok and Renno, 2008; Zheng et al., 2003), whereas  
19 recent field measurements found a dramatic increase in dust concentration **during**  
20 **dust storms** (up to a factor of 10) by E-field (Esposito et al., 2016), suggesting that E-  
21 field might enhance saltation mass flux during dust storms. This is probably because  
22 **only the vertical component of the E-field (i.e. 1-D) should be considered in pure**  
23 **saltation**, but there also in fact exist streamwise and spanwise components of E-field  
24 in dust events. For example, Jackson and Farrell (2006) recorded the horizontal  
25 component of the E-field of up to 120 kV m<sup>-1</sup> in dust devils. Zhang and Zheng (2018)  
26 also found the streamwise and spanwise components (termed horizontal component)  
27 of the E-field of up to 150 kV m<sup>-1</sup> in dust storms. Hence, E-field is actually three-  
28 dimensional (3-D) **during dust storms**. In many cases, the magnitude of the horizontal  
29 component is larger than that of the vertical component (**Bo and Zheng, 2013; Zhang**

1 and Zheng, 2018). The horizontal component should therefore not be neglected when  
2 evaluating the role of E-field in saltation during dust storms.

3 Most field observations, such as Schmidt et al. (1998) and Bo et al. (2014), have  
4 studied the electrical properties of sand particles in dust events. However, many  
5 environmental (lurking) factors, such as relative humidity, soil moisture, surface crust,  
6 etc., cannot be fully controllable (recorded) in these field observations. The  
7 uncertainties in the field observations provide motivation for numerical studies of the  
8 particle triboelectric charging in saltation. In addition, unlike pure saltation, the dust  
9 storm is a very complex dusty phenomenon that is made up by numerous polydisperse  
10 particles embedded in a high Reynolds-number turbulent flow. Such high complexity  
11 of dust storms challenges the accurate simulation of 3-D E-field in dust storms. It is  
12 therefore more straightforward to characterize 3-D E-field experimentally.

13 In this study, we evaluate the effects of 3-D E-field on saltation during dust storms  
14 by combining measurements and modelling. To reveal the properties of 3-D E-field, we  
15 simultaneously measured the 3-D E-fields in the sub-meter layer from 0.05 to 0.7 m  
16 above the ground during a dust storm. Such vertical profile of the 3-D E-field in the  
17 sub-meter layer has not been previously characterized. To reveal how 3-D E-field  
18 affects saltation during dust storms, we develop a comprehensive numerical model of  
19 particle triboelectric charging in saltation. In this model, the charge transfers between  
20 contacting particles are explicitly calculated, but the 3-D E-field is formulated directly  
21 based on the data measured in our measurements, due to its huge challenges in  
22 modelling. The effects of various important parameters, such as the density of charged  
23 species and the height-averaged time-varying mean of the 3-D E-field, are also  
24 investigated and described herein.

## 26 **2. Field campaign**

### 27 **2.1 Observational set-up and uncertainty**

28 We performed 3-D E-field measurements at the Qingtu Lake Observation Array  
29 (QLOA) site (approximately  $39^{\circ}12'27''$  N,  $103^{\circ}40'03''$  E, as shown in Fig. 1a), in

1 May 2014. The measured physical quantities include: wind velocities at four heights  
2 measured by the sonic anemometers (CSAT3B, Campbell Scientific, Inc.) with 50 Hz  
3 sampling frequency; number of saltating particle passing through the measurement  
4 area (2 mm×25 mm) per second at six heights measured by sand particle counter (SPC-  
5 91, Niigata Electric Co., Ltd.) with 1 Hz sampling frequency, thus providing an  
6 estimation of the size distribution of saltating particles, saltation mass flux, and  
7 saltation height (Text S1 in the Supplement); 3-D E-field at five heights measured by  
8 the vibrating-reed E-field mill (VREFM, developed by Lanzhou University) with 1 Hz  
9 sampling frequency. The layout of all instruments is shown in Fig. 1b. All instruments  
10 are powered by solar panels.

11 A detailed description of VREFM can be found in the Supplement of Zhang et al.  
12 (2017), but we describe it here briefly. The working principle of VREFM is based on the  
13 dynamic capacity technique, as illustrated in the inset of Fig. 1b. Unlike traditional  
14 atmospheric electric field mill, VREFM is composed of only one vibrating electrode. As  
15 the electrode oscillates, it charges and discharges periodically. The magnitude of the  
16 induced electric current  $i(t)$  is proportional to the ambient E-field intensity  $E$   
17 (Zhang et al., 2017), i.e.

$$18 \qquad \qquad \qquad 19 \qquad \qquad \qquad i(t) \propto E\omega \cos(\omega t) \qquad (1)$$

20  
21 where  $\omega$  is the vibration frequency of the electrode. The induced electric current is  
22 then converted to an output voltage signal, which is linearly proportional to the  
23 ambient E-field, through functional modules within VREFM. In addition, the length and  
24 diameter of the VREFM sensor are approximately 2.5 cm and 7 cm, respectively. This  
25 small size sensor allows us to measure E-field very close to ground but do not disturb  
26 the ambient E-field significantly.

27 The measurement uncertainties in our field campaign are threefold: wind velocity  
28 (CSAT3B), particle mass flux (SPC-91), and E-field (VREFM). The CSAT3B is factory  
29 calibrated with an accuracy of  $\pm 8 \text{ cm s}^{-1}$ . And the SPC-91 is factory calibrated by a set

1 of filamentation wires of equivalent diameters from 0.138 to 0.451 mm, with an  
2 uncertainty of  $\pm 0.015$  mm. The VREFM used in the field measurements is carefully  
3 calibrated and selected in our lab by a parallel-plate E-field calibrator (Zhang et al.,  
4 2017), and its maximum uncertainties range from  $\sim 1.38\%$  to  $\sim 2.24\%$  (see Text S2 in  
5 the Supplement).

6

## 7 **2.2 Data analysis**

8 In general, the actual wind direction exits a specific angle from the prevailing wind  
9 direction. A projection step is therefore needed to obtain the streamwise E-field,  $E_1$ ,  
10 and spanwise E-field,  $E_2$ . For example,  $E_1$  is equal to the sum of the projection of the  
11 measured  $E_x$  and  $E_y$  (E-field in the direction of  $x$  and  $y$  axes, as shown in Fig. 1b)  
12 to the streamwise wind direction.

13 After completing the projection step, we then perform the following steps  
14 sequentially to reveal the pattern of 3-D E-field in the sub-meter layer: (1) estimating  
15 time-varying mean values of E-field; (2) computing height-averaged time-varying mean  
16 in the measurement region from 0.05 to 0.7 m above the ground; (3) normalizing E-  
17 field by height-averaged mean values; and (4) finally fitting the vertical profiles of  
18 normalized E-field by the 3-order polynomial functions. It is worth noting that the  
19 measured time series in dust storms are generally non-stationary when viewed as a  
20 whole (e.g. Zhang and Zheng, 2018). In such cases, the statistical values are time-  
21 varying. Here, we use the discrete wavelet transform (DWT) method (Daubechies,  
22 1990) and the ensemble empirical mode decomposition (EEMD) method (Wu and  
23 Huang, 2009), which are widely used in various geophysical studies (e.g. Grinsted et  
24 al., 2004; Huang and Wu, 2008; Wu et al., 2011), to estimate the time-varying mean  
25 values of the measured non-stationary 3-D E-field data. We select these two methods  
26 since the DWT with higher orders of Daubechies wavelet (e.g. db10) and the EEMD can  
27 extract a reasonable and physically meaningful time-varying mean (Su et al., 2015).  
28 Each step for revealing the 3-D E-field pattern is described in detail as follows:

29 The DWT uses a set of mutually orthogonal wavelet basis functions, which are

1 dilated, translated and scaled versions of a mother wavelet, to decompose an E-field  
 2 series  $E$  into a series of successive octave band components (Percival and Walden,  
 3 2000), i.e.,

$$4 \quad E = \sum_{i=1}^N \psi_i + \chi_N \quad (2)$$

6  
 7 Where  $N$  is the total number of decomposition levels,  $\psi_i$  denotes the  $i$ -th level  
 8 wavelet detail component, and  $\chi_N$  represents the  $N$ -th level wavelet approximation  
 9 (or smooth) component. As  $N$  increases, the frequency contents become lower and  
 10 thus the  $N$ -th level approximation component could be regarded as the time-varying  
 11 mean values (e.g. Percival and Walden, 2000; Su et al., 2015). In this study, the DWT  
 12 decomposition is performed with the Daubechies wavelet of order 10 (db10) at level  
 13 10, and thus the 10-th order approximation component can be defined as the time-  
 14 varying mean:

$$15 \quad \bar{E} = \chi_{10} \quad (3)$$

17  
 18 which reflect the averages of the  $E$  series over a scale of  $2^{10}$  s (Percival and Walden,  
 19 2000).

20 On the other hand, according to the empirical mode decomposition (EMD)  
 21 method, the time series  $E$  can be decomposed as (Huang et al., 1998)

$$22 \quad E = \sum_{i=1}^N \xi_i + \eta_N \quad (4)$$

24  
 25 through a sifting process, where  $\xi_i$  are the intrinsic mode functions (IMFs), and  $\eta_N$   
 26 is a residual (which is the overall trend or mean). To reduce the end effects and mode  
 27 mixing in EMD, the EEMD method is proposed by Wu and Huang (2009). In EEMD, a

1 set of white noise series,  $w_j$  ( $j = 1, 2, \dots, N_e$ ), are added to the original signal  $E$ . Then,  
 2 each noise-added series is decomposed into IMFs followed by the same sifting process  
 3 as in EMD. Finally, the  $i$ -th EEMD component is defined as the ensemble mean of the  
 4  $i$ -th IMFs of the total of  $N_e$  noise-added series (see Wu and Huang, 2009 for details).

5 In this study, the time-varying mean values  $\bar{E}$  can be alternatively defined as the  
 6 sum of the last four EEMD components,  $\xi_{10}$  to  $\xi_{13}$ , and the residual,  $\eta_{13}$ , i.e.

$$7 \quad \bar{E} = \sum_{i=10}^{13} \xi_i + \eta_{13} \quad (5)$$

9  
 10 According to the above definitions, the time-varying mean can be synchronously  
 11 obtained by the DWT and EEMD methods. As an example, Fig. 2 shows the results of  
 12 DWT analysis (Fig. 2b) and EEMD decompositions (Fig. 2c) for an E-field time series  $E$   
 13 in our field campaign. It can be seen that DWT and EEMD can properly capture a similar  
 14 time-varying mean (Fig. 2a). This is because the EEMD is conceptually very similar to  
 15 the DWT and thus behaves as a “wavelet-like” filter bank (Flandrin, 2004). As shown in  
 16 Fig. 3, the frequencies contained in the DWT and EEMD components become  
 17 progressively lower, where the mean frequencies of  $\psi_{10}$  and  $\xi_9$  are  $7.69 \times 10^{-4}$  and  
 18  $7.24 \times 10^{-4}$  Hz, respectively. The time-varying means (defined as the summation of the  
 19 components below the dashed line in Fig. 3)  $\chi_{10}$  and  $\sum_{i=10}^{13} \xi_i + \eta_{13}$  show very close  
 20 mean frequencies of  $7.71 \times 10^{-6}$  and  $7.85 \times 10^{-6}$  Hz, respectively. We thus conclude that  
 21 such definitions in Eq. (3) and (5) can extract the time-varying mean over a certain  
 22 scale of about  $7.47 \times 10^{-4}$  Hz (below the dashed line in Fig. 3).

23 Since the 3-D E-field are measured at five heights in our field campaign, we thus  
 24 define the height-averaged time-varying mean values as

$$25 \quad \langle \bar{E}_i \rangle = \left| \frac{1}{(0.7 - 0.05)} \int_{0.05}^{0.7} \bar{E}_i dz \right| \quad (6)$$

27



1 in the range of 0.05 to 0.7 m height, in order to normalize the E-field data by a unified  
2 quantity. Further, the E-field data can be normalized as

3

$$4 \quad E_i^* = \frac{E_i}{\langle E_i \rangle} \quad (7)$$

5

6 Additionally, to obtain the dimensionless vertical profile of 3-D E-field, the height  $z$   
7 should also be a dimensionless parameter. Here, the dimensionless height  $z^*$  is  
8 defined as the ratio of height  $z$  to the mean saltation height  $\bar{z}_{salt}$  during the whole  
9 observed dust storm, i.e.

10

$$11 \quad z^* = \frac{z}{\bar{z}_{salt}} \quad (8)$$

12

13 where the saltation height  $z_{salt}$  during a certain time interval is defined as the height  
14 below which 99 % of the total mass flux is present and can be estimated based on the  
15 measured SPC-91 data (see Text S1 in the Supplement for more details).

16 Finally, the dimensionless vertical profiles of 3-D E-field at different periods are  
17 together fitted by the 3-order polynomial functions:

18

$$19 \quad E_i^*(z^*) = a_{0,i} + a_{1,i}z^* + a_{2,i}(z^*)^2 + a_{3,i}(z^*)^3, \quad i = 1,2,3 \quad (9)$$

20

21 where  $i = 1, 2,$  and  $3$  correspond to the streamwise, spanwise, and vertical  
22 components, respectively.

23

### 24 **3. Saltation model**

25 For modelling steady-state saltation, there are four primary processes, including  
26 (1) particle saltating motion, (2) particle-particle midair collisions, (3) particle-bed  
27 collisions, and (4) particle-wind momentum coupling (Dupont et al., 2013; Kok and  
28 Renno, 2009). Also, the changes in both momentum and electrical charge of each

1 particle are taken into account in the particle-particle midair and particle-bed collisions.  
 2 To avoid overestimating midair collisions in 2-D simulation (Carneiro et al., 2013), we  
 3 simulate saltation trajectories in a real 3-D domain. We use the discrete element  
 4 method (DEM), which explicitly simulates each particle motion and describes the  
 5 collisional forces between colliding particles encompassing normal and tangential  
 6 components, to advance the evaluation of the effects of particle midair collisions. In  
 7 the following subsections, we will describe each process in detail.

8

### 9 **3.1 Size distribution of particle sample**

10 Granular materials in natural phenomena, such as sand, aerosols, pulverized  
 11 material, seeds of crops, etc., are made up of discrete particles with a wide range of  
 12 sizes ranging from a few micrometers to millimeters. The log-normal distribution is  
 13 generally used to approximate the size distribution of the sand sample (Dupont et al.,  
 14 2013; Marticorena and Bergametti, 1995). Thus, the mass distribution function of a  
 15 sand sample with two parameters, average diameter  $d_m$ , and geometric standard  
 16 deviation  $\sigma_p$ , can be written as

17

$$18 \quad \frac{dM(d_p)}{d\ln(d_p)} = \frac{1}{\sqrt{2\pi}\ln(\sigma_p)} \exp\left\{-\frac{[\ln(d_p) - \ln(d_m)]^2}{2[\ln(\sigma_p)]^2}\right\} \quad (10)$$

19

### 20 **3.2 Equations of saltating particles motion**

21 The total force acting on a saltating particle consists of three distinct interactions  
 22 (Minier, 2016). The first one refers to the wind-particle interaction, which is dominated  
 23 by the drag force with lifting forces such as Saffman force and Magnus force being of  
 24 secondary importance (Dupont et al., 2013; Kok and Renno, 2009). The second  
 25 interaction refers to the particle-particle collisional forces or cohesion caused by  
 26 physical contact between particles. Such interparticle collisional forces can be  
 27 described as a function of the overlaps between the colliding particles. The third  
 28 interaction refers to the forces due to external fields such as gravity and E-field. In this

1 study, in addition to the drag force, we also take into account the Magnus force  
 2 because of the remarkable rotation of saltating particles on the order of 100-1000 rev  
 3 s<sup>-1</sup> (Xie et al., 2007). The effects of electrostatic forces on particle motion, which are  
 4 significant for large wind velocity (Schmidt et al., 1998; Zheng et al., 2003), are also  
 5 taken into account. Consequently, the full governing equations of saltating particles  
 6 can be written as

7

$$8 \quad m_{p,i} \frac{d\vec{u}_{p,i}}{dt} = \vec{F}_i^d + \vec{F}_i^m + \sum_j (\vec{F}_{ij}^n + \vec{F}_{ij}^t) + m_i \vec{g} + \zeta_{p,i} \vec{E} \quad (11a)$$

$$9 \quad I_i \frac{d\vec{\omega}_{p,i}}{dt} = \vec{M}_i^{w-p} + \sum_j (\vec{M}_{ij}^c + \vec{M}_{ij}^r) \quad (11b)$$

10

11 where  $m_{p,i}$  is the mass of the  $i$ -th particle;  $\vec{u}_{p,i}$  is the velocity of the particle;  $\vec{F}_i^d$  is  
 12 the drag force;  $\vec{F}_i^m$  is the Magnus force;  $\vec{F}_{ij}^d$  and  $\vec{F}_{ij}^t$  are the normal and tangential  
 13 collisional forces from the  $j$ -th particle, respectively;  $\vec{g}$  is the gravitational  
 14 acceleration;  $\zeta_{p,i}$  is the charge-to-mass ratio of the sand particles and is altered  
 15 during every collision (see section 3.4);  $\vec{E}$  is the 3-D E-field given by our  
 16 measurements;  $I_i$  is the moment of inertia;  $\vec{\omega}_{p,i}$  is the angular velocity of the  
 17 particle;  $\vec{M}_i^{w-p}$  is the torque caused by the wind on the particle;  $\vec{M}_{ij}^c$  and  $\vec{M}_{ij}^r$  are  
 18 the tangential torque due to the tangential component of the particle collisional forces  
 19 and the rolling resistance torque, respectively. The summation  $\Sigma$  represents  
 20 considering all particles that are in contact with the  $i$ -th particle.

21

### 22 **3.2.1 Wind-particle interactions**

23 In the absence of saltating particles, the mean wind profile over a flat and  
 24 homogeneous surface is well approximated by the log-law (Anderson and Haff, 1988)

25

$$26 \quad u_m(z) = \frac{u_*}{\kappa} \ln \frac{z}{z_0} \quad (12)$$

1

2 where  $u_m$  is the mean streamwise wind speed;  $z$  is the height above the surface;  
 3  $u_*$  is the friction velocity;  $\kappa \approx 0.41$  is the von Kármán constant;  $z_0$  is the  
 4 aerodynamic roughness, which varies substantially form different flow conditions and  
 5 can be approximately estimated as  $d_m/30$  for the aeolian saltation on Earth (e.g.  
 6 Carneiro et al., 2013; Kok et al., 2012). In the presence of saltation, due to the  
 7 momentum coupling between the saltating particles and wind flow, the modified wind  
 8 speed gradient can be written as follows for steady-state and horizontally-  
 9 homogeneous saltation (e.g. Kok and Renno, 2009; Pähtz et al., 2015)

10

$$11 \quad \frac{du_m(z)}{dz} = \frac{u_*}{\kappa z} \sqrt{1 - \frac{\tau_p(z)}{\rho_a u_*^2}} \quad (13)$$

12

13 where  $\rho_a$  is the air density,  $\tau_p(z)$  is the particle momentum flux and can be  
 14 numerically determined by (Carneiro et al., 2013; Shao, 2008)

15

$$16 \quad \tau_p(z) = -\frac{\sum m_{p,i} u_{p,i} w_{p,i}}{L_x L_y \Delta z} \quad (14)$$

17

18 with  $L_x$ ,  $L_y$ , and  $\Delta z$  being the streamwise-, spanwise-width of the computational  
 19 domain, and vertical grid size, respectively;  $u_{p,i}$  and  $w_{p,i}$  are the streamwise and  
 20 vertical components of particle velocity. The summation in Eq. (14) is performed on  
 21 the particles located in the range of  $[z, z + \Delta z]$ . Once saltating particle trajectories are  
 22 known, the wind profile can be determined through integrating Eq. (13) with the no-  
 23 slip boundary condition  $u_m = 0$  at  $z = z_0$ .

24

25 Since sand particles are much heavier than the air and are well smaller than the  
 26 Kolmogorov scales, the drag force is the dominant force affecting particle motion,  
 27 which is expressed by (Anderson and Haff, 1991)

27

$$\vec{F}_i^d = -\frac{\pi d_p^2}{8} \rho_a C_d \vec{u}_r |\vec{u}_r| \quad (15)$$

where  $d_p$  is the diameter of the particle;  $C_d$  is the drag coefficient; and  $\vec{u}_r = \vec{u}_p - \vec{u}_w$  is the particle-to-wind relative velocity. The drag coefficient  $C_d$  is a function of the particle Reynolds number,  $Re_p = \rho_a |\vec{u}_r| d_p / \mu$ , where  $\mu$  is the dynamic viscosity of the air. We calculate the drag coefficient by an empirical relation  $C_d = \left[ (32/Re_p)^{2/3} + 1 \right]^{3/2}$ , which is applicable to the regimes from Stokes flow  $Re_p \ll 1$  to high Reynolds number turbulent flow (Cheng, 1997).

Additionally, we also account for the effects of particle rotation on particle motion using the Magnus force expressed as (Anderson and Hallet, 1986; Loth, 2008; White and Schulz, 1977)

$$\vec{F}_i^m = \frac{\pi d_p^2}{8} \rho_a C_m (\vec{\omega}_{p,i} \times \vec{u}_r) \quad (16)$$

where  $C_m$  is a normalized spin lift coefficient depended on the particle Reynolds number and the circumferential speed of the particle. The torque acting on a particle caused by wind flow is calculated from (Anderson and Hallet, 1986; Kok and Renno, 2009; Shao, 2008)

$$\vec{M}_i^{w-p} = \pi \mu d_i^3 \left( \frac{1}{2} \frac{du_m}{dz} - \vec{\omega}_i \right) \quad (17)$$

### 3.2.2 Particle-particle midair collisions

Under moderate conditions, saltation is a dilute flow in which the particle-particle collisions are negligible. However, as wind velocity increases, midair collisions become increasingly pronounced, especially in the near-surface region (Sørensen and McEwan, 1996). Previous studies found that the probability of midair collisions of saltating particles almost increased linearly with wind speed (Huang et al., 2007) and such collisions indeed enhanced the total mass flux substantially (Carneiro et al., 2013). For

1 spherical particles, one of the most commonly-used collisional force model is the  
 2 nonlinear viscoelastic model, consisting of two components, i.e. elastic and viscous  
 3 forces (Brilliantov et al., 1996; Haff and Anderson, 1993; Silbert et al., 2001; Tuley et  
 4 al., 2010).

5 Considering two spherical particles  $i$  and  $j$  with diameters  $d_i$  and  $d_j$ , and  
 6 position vectors  $\vec{x}_i$  and  $\vec{x}_j$ , are in contact with each other. The relative velocity  $\vec{v}_{ij}$   
 7 at the contact point and its normal and tangential components,  $\vec{v}_{ij}^n$  and  $\vec{v}_{ij}^t$ , are  
 8 respectively defined as (Norouzi et al., 2016; Silbert et al., 2001)

9

$$10 \quad \vec{v}_{ij} = \vec{u}_{p,i} - \vec{u}_{p,j} + 0.5(d_i\vec{\omega}_{p,i} + d_j\vec{\omega}_{p,j}) \times \vec{n}_{ij} \quad (18a)$$

$$11 \quad \vec{v}_{ij}^n = (\vec{v}_{ij} \cdot \vec{n}_{ij})\vec{n}_{ij} \quad (18b)$$

$$12 \quad \vec{v}_{ij}^t = \vec{v}_{ij} - \vec{v}_{ij}^n \quad (18c)$$

13

14 where  $\vec{n}_{ij} = (\vec{x}_j - \vec{x}_i)/|\vec{x}_j - \vec{x}_i|$  is the unit vector in the direction from the center  
 15 of particle  $i$  point toward the center of particle  $j$ . Suppose that these colliding  
 16 particles having identical mechanical properties with Young's modulus  $Y$ , shear  
 17 modulus  $G$ , and Poisson's ratio  $\nu$ , and thus the normal collisional force can be  
 18 calculated by (Brilliantov et al., 1996; Silbert et al., 2001)

19

$$20 \quad \vec{F}_{ij}^n = -\frac{4}{3}Y^*\sqrt{R^*}\delta_n^{3/2}\vec{n}_{ij} - 2\sqrt{\frac{5}{6}m^*S_n\beta}v_n\vec{n}_{ij} \quad (19)$$

21

22 where  $Y^* = Y/2/(1 - \nu^2)$  is the equivalent Young's modulus;  $\delta_n = 0.5(d_i + d_j) -$   
 23  $|\vec{x}_i - \vec{x}_j|$  is the normal overlap;  $m^* = m_i m_j / (m_i + m_j)$  is the equivalent particle  
 24 mass;  $S_n = 2Y^*\sqrt{R^*\delta_n}$  is the normal contact stiffness;  $R^* = d_i d_j / 2 / (d_i + d_j)$  is  
 25 the equivalent particle radius;  $\beta$  is related to the coefficient of restitution  $e_n$  by the  
 26 relationship  $\beta = \ln e_n / \sqrt{(\ln e_n)^2 + \pi^2}$ ; and  $v_n = \vec{v}_{ij} \cdot \vec{n}_{ij}$ . The first term on the right-

1 hand side of Eq. (18) represents the elastic force described by Hertz's theory, and the  
 2 second term represents the viscous force reflecting the inelastic collisions between  
 3 sand particles. Similarly, the tangential collisional force, which is limited by the  
 4 Coulomb friction, is given as (Brilliantov et al., 1996; Silbert et al., 2001)

$$\vec{F}_{ij}^t = \begin{cases} -8G^* \sqrt{R^* \delta_n} \delta_t \vec{t}_{ij} - 2 \sqrt{\frac{5}{6}} m^* S_t \beta v_t \vec{t}_{ij}, & \text{if } |\vec{F}_{ij}^t| \leq \gamma_s |\vec{F}_{ij}^n| \\ -\gamma_s |\vec{F}_{ij}^n| \vec{t}_{ij}, & \text{if } |\vec{F}_{ij}^t| > \gamma_s |\vec{F}_{ij}^n| \end{cases} \quad (20)$$

7  
 8 where  $G^* = G/2/(2 - \nu)$  is the equivalent shear modulus;  $\delta_t$  is the tangential  
 9 overlap;  $\vec{t}_{ij} = \vec{v}_{ij}^t / |\vec{v}_{ij}^t|$  is the tangential unit vector at the contact point;  $S_t =$   
 10  $8G^* \sqrt{R^* \delta_n}$  is the tangential stiffness;  $v_t = \vec{v}_{ij} \cdot \vec{t}_{ij}$ ; and  $\gamma_s$  is the coefficient of static  
 11 friction. The torque on the  $i$ -th particle arising from the  $j$ -th particle collisional force  
 12 is defined as (Haff and Anderson, 1993)

$$\vec{M}_{ij}^c = 0.5 d_i \vec{n}_{ij} \times \vec{F}_{ij}^t \quad (21)$$

13  
 14  
 15  
 16 To account for the significant rolling friction, we apply a rolling resistance torque  
 17 (Ai et al., 2011)

$$\vec{M}_{ij}^r = -\gamma_r R^* |\vec{F}_{ij}^n| \vec{\omega}_{ij} \quad (22)$$

18  
 19  
 20  
 21 on each colliding particle, where  $\mu_r$  is the coefficient of rolling friction, and  $\vec{\omega}_{ij} =$   
 22  $(\vec{\omega}_{p,i} - \vec{\omega}_{p,j}) / |\vec{\omega}_{p,i} - \vec{\omega}_{p,j}|$  is the unit vector of relative angular velocity.

### 23 24 **3.3 Particle-bed collisions**

25 As a saltating particle collides with the sand bed, it has not only a chance to

1 rebound but also may eject several particles from the sand bed. For simplicity, we use  
 2 a probabilistic representation, termed as “splash function”, to describe the particle-  
 3 bed interactions quantitatively (Kok et al., 2012; Shao, 2008). Currently, the splash  
 4 function is primarily characterized by wind-tunnel and numerical simulations (e.g.  
 5 Anderson and Haff, 1991; Haff and Anderson, 1993; Huang et al., 2017; Rice et al.,  
 6 1996). The rebounding probability of a saltating particle colliding with the sand bed is  
 7 approximately by (Anderson and Haff, 1991)

8

$$9 \quad P_{reb} = 0.95[1 - \exp(-v_{imp})] \quad (23)$$

10

11 where  $v_{imp}$  is the impact speed of the saltating particle. The kinetic energy of the  
 12 rebounding particles is taken as  $0.45 \pm 0.22$  of the impact particle (Kok and Renno,  
 13 2009). The rebounding angles  $\theta$  and  $\varphi$ , as depicted in Fig. 3a, obey an exponential  
 14 distribution with a mean value of  $40^\circ$ , i.e.  $\theta \sim \text{Exp}(40^\circ)$ , and a normal distribution  
 15 with parameters  $0 \pm 10^\circ$ , i.e.  $\varphi \sim \text{N}(0^\circ, 10^\circ)$ , respectively (Dupont et al., 2013; Kok  
 16 and Renno, 2009).

17 It is reasonable to assume that the number of ejected particles depends on the  
 18 impact speed and its cross-sectional area. Thus, the number of ejected particles from  
 19 the  $k$ -th particle bin is (Kok and Renno, 2009)

20

$$21 \quad N_k = \frac{0.02}{\sqrt{gD_{250}}} \frac{D_{imp}}{D_{eje}^k} p_k v_{imp} \quad (24)$$

22

23 where  $D_{250} = 0.25 \times 10^{-4}$  m is a reference diameter;  $D_{imp}$  and  $D_{eje}^k$  are the  
 24 diameter of the impact and ejected particles, respectively; and  $p_k$  is the mass  
 25 fraction of the  $k$ -th particle bin. The speed of the ejected particles obeys an  
 26 exponential distribution with mean value taken as  $0.6[1 - \exp(-v_{imp}/40/\sqrt{gD_{250}})]$   
 27 (Kok and Renno, 2009). Similar to the rebound process, the ejected angles  $\theta$  and  $\varphi$



1 are assumed to be  $\theta \sim \text{Exp}(50^\circ)$  and  $\varphi \sim N(0^\circ, 10^\circ)$ .

### 3 3.4 Particle charge exchanges

4 In this study, the calculation of the charge transfer between sand particle  
5 collisions is based on the asymmetric contact model, assuming that the electrons  
6 trapped in high energy states on one particle surface can relax to the other particle  
7 surface (Hu et al., 2012; Kok and Lacks, 2009). Thus, the net increment of the charge  
8 of particle  $i$  after colliding with particle  $j$ ,  $\Delta q_{ij}$ , can be determined by

$$10 \quad \Delta q_{ij} = -e(\rho_h^j S_j - \rho_h^i S_i) \quad (25)$$

11  
12 where  $e = 1.602 \times 10^{-19}$  C is the elementary charge;  $\rho_h^i$  is the density of the  
13 electrons trapped in the high energy states on the surface of particle  $i$  (assuming that  
14 all particles have an identical initial value  $\rho_h^0$ ), which is modified as

$$16 \quad \rho_{h,i}^{\text{after}} = \rho_{h,i}^{\text{before}} - \frac{\Delta q_{ij}}{e\pi d_i^2} \quad (26)$$

17  
18 due to collisions between particle  $i$  and  $j$ ;  $S_i$  is the particle contact area, which can  
19 be approximately calculated as a line integral along the contact path  $L_i$  of particle  $i$

$$21 \quad S_i = 2 \int_{L_i} \sqrt{R^* \delta_n} dl_i \quad (27)$$

22  
23 where  $dl_i$  is the differential of the contact length. In general, when two particles are  
24 in contact with each other, the relative sliding motion between the two particles  
25 results in two unequal contact areas  $S_i$  and  $S_j$ , thus producing net charge transfer  
26  $\Delta q_{ij}$  between the two particles. If the particle's net electrical charge is known, its  
27 charge-to-mass ratio can be easily determined.

### 3.5 Particle-phase statistics

Similar to particle momentum flux (i.e. Eq. 14), particle horizontal mass flux  $q$ , total mass flux  $Q$ , mean particle mass concentration  $m_c$ , and mean particle charge-to-mass ratio  $\langle \zeta_p \rangle$  can be numerically determined by (Carneiro et al., 2013; Dupont et al., 2013)

$$q(z) = \frac{\sum m_{p,i} u_{p,i}}{L_x L_y \Delta z} \quad (28a)$$

$$Q = \frac{\sum m_{p,i} u_{p,i}}{L_x L_y} \quad (28b)$$

$$m_c(z) = \frac{\sum m_{p,i}}{L_x L_y \Delta z} \quad (28c)$$

$$\langle \zeta_p \rangle(z) = \frac{\sum \zeta_{p,i} m_{p,i} u_{p,i}}{\sum m_{p,i} u_{p,i}} \quad (28d)$$

where the summation  $\sum$  is performed over the saltating particles located in the range of  $[z, z + \Delta z]$  for  $q$ ,  $m_c$ , and  $\langle \zeta_p \rangle$ , but it is performed over all saltating particles for  $Q$ . The  $\langle \zeta_p \rangle$  is defined as the ratio of charge flux and mass flux in the range of  $[z, z + \Delta z]$ .

### 3.6 Model implementation

We consider polydisperse soft-spherical sand particles having log-normal mass distribution in a 3-D computational domain  $0.5 \text{ m} \times 0.1 \text{ m} \times 1.0 \text{ m}$  (as shown in Fig. 4a), with periodic boundary condition in the  $x$  and  $y$  directions. Here, the upper boundary is set to be high enough so that the particle escapes from the upper boundary can be avoided. To reduce the computational cost, the spanwise dimension is chosen as  $L_y = 0.1$ , since the saltating particles are mainly moving along the streamwise direction.

As shown in Fig. 4b, the model is initiated by randomly releasing 100 uncharged

1 particles, within the region below 0.3 m, and then such released particles begin to  
 2 move under the action of the initial log-law wind flow, triggering saltation through a  
 3 series of particle-bed collisions. We use cell-based collision searching algorithms,  
 4 which perform collision search for particles located in the target cell and its  
 5 neighboring cells, to find the midair colliding pairs. The random processes, particle-  
 6 bed collisions described previously, are simulated using a general method called the  
 7 inverse transformation. The particle motion and wind flow equations are integrated by  
 8 predictor-corrector method AB3AM4; that is, 3-order Adams-Bashforth method to  
 9 perform prediction and 4-order Adams-Moulton method to perform the correction.  
 10 One of the main advantages of using such multi-step integration method is that the  
 11 accuracy of results is not sensitive to the detection of exact moments of collision (Tuley  
 12 et al., 2010). The charge transfer between the colliding pairs is caused by their  
 13 asymmetric contact and can be determined by Eqs. (25)-(27). When calculating  
 14 particle-bed charge transfer, the bed is regarded as an infinite plane. According to the  
 15 law of charge conservation, the surface charge density of the infinite bed plane and  
 16 the newly ejected particles,  $\sigma$ , is (Kok and Renno, 2008; Zhang et al., 2014)

17

$$18 \quad \sigma = - \int_{z_0}^{+\infty} \rho_c(z) dz \quad (28)$$

19

20 where  $\rho_c$  is the space charge density. For modelling pure saltation, the E-field is  
 21 calculated by Gauss's law (e.g. Zhang et al., 2014). For modelling saltation during dust  
 22 storms, the 3-D E-field is directly formulated by Eq. (9) based on our field  
 23 measurements, as mentioned above. The variables used in this study are listed and  
 24 described in Table 1.

25

## 26 **4. Results**

### 27 **4.1. Vertical profiles of 3-D E-field**

28 On May 6, 2014, field measurements began at ~12:00 due to the limited power

1 supply by solar panels. As shown in Fig. 5, although the early stage of dust storm has  
 2 not been observed **completely**, we successfully recorded data of about 8 hours, which  
 3 is substantial enough to reveal the pattern of 3-D E-field. From Fig. 5, it can be seen  
 4 that, in general, the streamwise and spanwise components (up to  $\sim 80 \text{ kV m}^{-1}$ ) are  
 5 consistently larger than the vertical component of the E-field (up to  $\sim 40 \text{ kV m}^{-1}$ ). The  
 6 vertical profiles of the normalized streamwise, spanwise, and vertical components of  
 7 E-field are shown in Figs. 6a-6c, respectively. To the best of our knowledge, these data  
 8 are the first measured 3-D E-field data in the sub-meter layer during dust storms.  
 9 Numerous studies showed that the vertical component of E-field in pure saltation  
 10 decreased with increasing height (e.g., Kok and Renno, 2008; Schmidt et al., 1998;  
 11 Zhang et al., 2014). Interestingly, Fig. 6c shows that during dust storms, all normalized  
 12 components,  $E_1^*$  to  $E_3^*$ , decreases monotonically as height increases in the saltation  
 13 layer (i.e.  $z^* \leq 1$ ), similar to the pattern of vertical component in pure saltation.

14 As shown in Figs. 6a-6c, in different periods, each component of the normalized  
 15 3-D E-field roughly collapses on a single 3-order polynomial curve (with  $R^2=0.67-0.97$ ,  
 16 see Table 2 for details). This suggests that during dust storms, the 3-D E-field in the  
 17 sub-meter layer can be characterized as  $\langle \overline{E}_i \rangle E_i^*$ , where  $E_i^*$  represents the pattern of  
 18 the dimensionless E-field vertical profile (formulated by Eq. 9), and  $\langle \overline{E}_i \rangle$  represents  
 19 the height-averaged time-varying mean defined in Eq. (6). It is worth noting that the  
 20 E-field pattern  $E_i^*$  and their intensities  $\langle \overline{E}_i \rangle$  **are strongly dependent on** the saltation  
 21 conditions, such as dust mass loading, temperature, relative humidity (RH), etc. For  
 22 example, at given ambient temperature and RH, the mean E-field intensities  $\langle \overline{E}_i \rangle$   
 23 increases linearly with dust mass loading (e.g. Esposito et al., 2016; Zhang et al., 2017).  
 24 In addition, both  $E_i^*$  and  $\langle \overline{E}_i \rangle$  could vary from event to event, among them, the  
 25 saltation conditions are quite different. So far, a quantitative representation of  $\langle \overline{E}_i \rangle$  is  
 26 challenging due to its high complexity, and thus we regard it as a basic parameter in  
 27 the following sections for exploring the effects of 3-D E-field on saltation. The fitting

1 results of Eq. (9) are listed in Table 2, with coefficients as rounded to two decimals. The  
2 formulations of the 3-D E-field can be readily substituted into the numerical model (i.e.  
3 Eq. 11a).

#### 4 5 **4.2. Effects of particle-particle midair collisions on saltation**

6 Before quantifying the effects of 3-D E-field on saltation by our numerical model,  
7 we draw a comparison of several key physical quantities between the simulated results  
8 and measurements in the case of pure saltation, in order to ensure the convergence  
9 and validity of our numerical code, as shown in Figs. 7a-7c. It is clearly shown that the  
10 saltation eventually reaches a dynamic steady-state after  $\sim 4$  seconds. The number of  
11 the impacting particles ( $\sim 72$  grains) is equal to the sum of the rebounding ( $\sim 50$  grains)  
12 and the ejected particles ( $\sim 22$  grains) during the time interval of  $10^{-4}$  s. At steady-state,  
13 each impacting particle, on average, produces a single saltating particle, either by  
14 rebound or by ejection. As shown in Fig. 7b, the total mass flux is well predicted by our  
15 numerical model, and midair collisions enhance the total mass flux dramatically,  
16 especially for less particle viscous dissipation (i.e. large  $e_n$ ) and large friction velocity.  
17 As in previous studies (e.g. Haff and Anderson, 1993; Carneiro et al., 2013), the  
18 selected  $e_n$  is larger than 0.5 since the  $e_n$  of quartz sand particles has been  
19 expected to lie in the range of  $\sim 0.5-0.6$  (Haff and Anderson, 1993; Kok et al., 2012).  
20 Also, the predicted charge-to-mass ratios of saltating particles are widely distributed  
21 from  $-400$  to  $+60 \mu\text{C kg}^{-1}$ , consistent with the previous measurements of charge-to-  
22 mass ratio in pure saltation (Bo et al., 2014; Schmidt et al., 1998; Zheng et al., 2003).  
23 To our knowledge, so far there are no actual measurements of charge on a single sand  
24 particle in dust events. In the case of Fig. 7c, the magnitude of the simulated mean  
25 charge-to-mass ratio is around  $100 \mu\text{C kg}^{-1}$ , corresponding to a mean charge of  
26  $1.64 \times 10^{-12}$  C/particle. This is in accordance with the empirical values of  $10^{-14}-10^{-12}$   
27 C/particle (Merrison, 2012).

28 In addition to affecting sand transport, midair collisions also affect charge  
29 exchanges between saltating particles. When considering midair collisions, the charge-

1 to-mass ratio distribution shifts slightly toward zero as the wind velocity increases, as  
2 shown in Figs. 8a-8c. As wind speed increases, the difference of the charge-to-mass  
3 ratio distribution between the cases with and without midair collisions is increasingly  
4 notable. This is because the probability of midair collisions become more significant  
5 for larger wind speed (Sørensen and McEwan, 1996; Huang et al., 2007).

### 7 4.3. Effects of 3-D E-field on saltation

8 By substituting the formulations of the 3-D E-field (i.e.  $\langle \overline{E}_i \rangle E_i^*$ ,  $i = 1,2,3$ ) into our  
9 model (i.e. Eq. 11a), we then evaluate the effects of 3-D E-field on saltation during  
10 storms properly. As shown in Fig. 9a, compared to the case without E-field, the vertical  
11 component of the E-field (i.e. 1-D E-field) inhibits mass flux, in agreement with  
12 previous studies (Kok and Renno, 2008; Zheng et al., 2003). However, the mass flux is  
13 enhanced by 3-D E-field, causing the simulated value closer to our measured data.  
14 Such enhancement of mass flux by 3-D E-field can be qualitatively explained by the  
15 considerable enhancements of  $m_c$  below  $\sim 0.02$  m height (Fig. 10a) and  $\langle u_p \rangle$  in the  
16 range from 0.01 to 0.1 m height (Fig. 10b), due to the streamwise and spanwise  
17 components. Meanwhile, although the saltation height is not sensitive to E-field  
18 vertical component, 3-D E-field enhances the saltation height significantly and,  
19 therefore, makes the numerical prediction more accurate (Fig. 9b). This is because  
20 when considering the E-field vertical component, the mass flux profile is very similar  
21 to the case of no E-field consideration (Figs. 9a and 10). In contrast, 3-D E-field causes  
22 a distortion of the mass flux profile (as well as  $m_c$  and  $\langle u_p \rangle$ ), and thus alters saltation  
23 height significantly (Figs. 9a and 10).

24 Additionally, we also explore how the key parameter, density of charged species  
25  $\rho_h^0$ , affects saltation, as shown in Figs. 11a-11c. Since the height-averaged time-varying  
26 mean is strongly dependent on the ambient conditions such as temperature and RH,  
27 the height-averaged time-varying mean is set at two different levels. The predicted  
28 results show that, at each height-averaged time-varying mean level, the magnitude of  
29 the charge-to-mass ratio increases with increasing  $\rho_h^0$ , and then reaches a relatively

1 equilibrium value at approximately  $\rho_h^0 = 10^{18} \text{ m}^{-2}$  (Fig. 10a), thus leading to a  
 2 constant enhancement of total mass flux  $Q$  and saltation height  $z_{salt}$  (Figs. 10b and  
 3 10c). From Eqs. (25)-(26), it can be seen that the net charge transfer  $\Delta q_{ij}$  is  
 4 proportional to the initial density  $\rho_h^0$  so that  $\langle \zeta_p \rangle$  increases rapidly with increasing  
 5  $\rho_h^0$  for small values of  $\rho_h^0$ . However, for larger  $\rho_h^0$ ,  $\Delta q_{ij}$  is no longer proportional to  
 6  $\rho_h^0$  because  $\Delta q_{ij}$  is limited by the difference of the number of charged species (i.e.  
 7  $\rho_h^j S_j - \rho_h^i S_i$ ) between two colliding particles (Kok and Lacks, 2009). Fig. 11c shows a  
 8 peak of increase in  $z_{salt}$  at  $\rho_h^0$  of about  $10^{16}$ - $10^{17} \text{ m}^{-2}$ , because  $\langle \zeta_p \rangle$  also exhibits a  
 9 peak in the same range of  $\rho_h^0$ . In addition, the peak is more apparent in Fig. 11c. This  
 10 is because  $z_{salt}$  is very sensitive to mass flux profile. A little change in mass flux  
 11 profile can lead to an apparent change in  $z_{salt}$  (see Text S1 in the Supplement). For  
 12 the larger height-averaged time-varying mean, the enhancements of the total mass  
 13 flux  $Q$  and saltation height  $z_{salt}$  could exceed 20 % and 15 %, respectively.

14

## 15 **5. Discussion**

### 16 **5.1. Field measurements of 3-D E-field in the sub-meter layer**

17 To determine the effects of particle triboelectric charging on saltation precisely,  
 18 3-D E-field measurements in the saltation layer (i.e. sub-meter above the ground) is  
 19 required. Although the E-field measurements, such as Bo and Zheng (2013), Esposito  
 20 et al. (2016), Kamra (1972), Rudge (1913), Williams et al. (2009), and Zhang et al. (2017)  
 21 in dust storms are numerous, 3-D E-field in the sub-meter layer have not been studied  
 22 so far. This is because the traditional atmospheric E-field sensors, such as CS110 sensor  
 23 manufactured by Campbell Scientific, Inc., have dimensions of  $15.2 \times 15.2 \times 43.2 \text{ cm}^3$   
 24 (e.g. Esposito et al., 2016; Yair et al., 2016), which is too large compared to the height  
 25 of saltation layer. Thus, it will lead to significant disturbances of the ambient E-field.  
 26 Fortunately, the diameter of the VREFM sensor developed by Lanzhou University is  
 27 only 2.5 cm and thus could considerably eliminate the E-field disturbances (Zhang et  
 28 al., 2017; Zheng, 2013). In this study, using the VREFM sensors, we have measured and

1 characterized the 3-D E-field from 0.05 to 0.7 m height during dust storms, which can  
2 provide valuable data for investigating the mechanisms of particle triboelectric  
3 charging in saltation.

4 In E-field data analysis, the E-field is normalized by its time-varying mean **over a**  
5 **certain timescale**, which can be extracted by the DWT and EEMD methods with  
6 negligible end effects and mode mixing (Percival and Walden, 2000; Wu and Huang,  
7 2009). At the same time, since the saltation height  $z_{salt}$  slightly varies with time (i.e.  
8  $0.172 \pm 0.0343$  m, see Fig. S3 in the supplement), the height  $z$  above the ground is  
9 normalized by the mean saltation height  $\bar{z}_{salt}$ . Note that we calculate the saltation  
10 height and mass flux over every 30-min time interval because the sufficiently long  
11 period is needed to capture all scales of turbulence (Martin and Kok, 2017; Sherman  
12 and Li, 2012). The 3-D E-field pattern is finally characterized as the 3-order polynomials,  
13 but it is only valid in the range that is not too far beyond the measurement points.  
14 Additionally, the 3-D E-field pattern of dust storms may vary event to event, because  
15 it is strongly related to the driving mechanisms of dust storms, such as monsoon winds,  
16 squall lines, and thunderstorms (Shao, 2008), and ambient conditions, such as  
17 temperature and relative humidity (Esposito et al., 2016; Zhang and Zheng, 2018).  
18 Although the 3-D E-field pattern revealed in this study may not be a universal feature,  
19 the proposed E-field data analysis method can be easily applied to other cases.

## 21 **5.2. Potential mechanisms for generating intense horizontal E-field in dust storms**

22 Like many previous studies, the E-field can be simplified to 1-D (i.e. vertical  
23 component) in pure saltation (e.g. Kok and Renno, 2008), since in such cases the  
24 magnitude of the streamwise and spanwise components is much less than that of  
25 vertical component (Zhang et al., 2014). However, during dust storms, the streamwise  
26 and spanwise components of the E-field are consistently larger than the vertical  
27 component, as mentioned previously. E-field is therefore 3-D **in dust storms**. In  
28 contrast to the vertical component which is closely related to the total mass loading  
29 (Esposito et al., 2016; Williams et al., 2009), **the intense streamwise and spanwise**



1 components of the E-field in dust storms may be aerodynamically created by the  
2 unsteady wind flows (Zhang et al., 2014) and turbulent fluctuations (Cimarelli et al.,  
3 2013; Renzo and Urzay, 2018). It is well-known that dust storm is a polydisperse (having  
4 dust particles with diameters from  $<10\ \mu\text{m}$  to  $\sim 500\ \mu\text{m}$ ) particle-laden turbulent flow  
5 at very high-Reynolds-number (up to  $\sim 10^8$ ). The wind flow in dust storms is certainly  
6 unsteady and random. Numerical simulation by Zhang et al. (2014) showed that the  
7 unsteady incoming flow could lead to the nonuniform transport of charged particles  
8 in the streamwise direction and thus resulted in fluctuating streamwise and vertical E-  
9 fields. In addition to unsteadiness, recent direct numerical simulation (Renzo and Urzay,  
10 2018) and laboratory experiment (Cimarelli et al., 2013) of particle-laden turbulent  
11 flows demonstrated that the generation of 3-D E-field could be caused by turbulent  
12 fluctuations. That is, the negatively charged small particles are affected by local  
13 turbulence and tend to accumulate in the interstitial regions between vortices, while  
14 the positively charged larger particles are unresponsive to turbulent fluctuations and  
15 are more uniformly distributed than the smaller (Cimarelli et al., 2013; Renzo and Urzay,  
16 2018). We thus reasonably expect that the negatively charged finer dust particles ( $<10\ \mu\text{m}$ )  
17 accumulate in specific regions, while the positively charged coarser sand particles  
18 ( $>100\ \mu\text{m}$ ) are more uniformly distributed due to its large inertia. Doubtless, such  
19 charge segregation could produce 3-D E-field (e.g. Renzo and Urzay, 2018). To sum up,  
20 the generating mechanisms responsible for the streamwise and spanwise E-fields in  
21 dust storms are probably the charge segregation caused by unsteady wind flows and  
22 turbulent fluctuations.

23         Additionally, one possible explanation for the intense streamwise and spanwise  
24 E-fields is that there exists large- and very-large-scale motions in atmospheric surface  
25 flows, leading to a large extent charge segregation in the streamwise and spanwise  
26 directions. In atmospheric surface layer flows, the largest vortices or coherent motions  
27 of the wind flows are found to be compared to the boundary layer thickness ( $\sim 60\text{-}200\ \text{m}$ )  
28 (Kunkel and Marusic, 2006; Hutchins et al., 2012). This may lead to a phenomenon  
29 that the charged particles are more nonuniformly distributed (over a larger spatial

1 scale) in the streamwise and spanwise directions than in the vertical direction.  
2 Accordingly, the intensity of the streamwise and spanwise E-fields is probably larger  
3 than that of the vertical E-field.

### 5 5.3. Particle-particle triboelectric charging resolved model

6 Although most physical mechanisms, such as asymmetric contact, polarization by  
7 external E-fields, statistical variations of material properties and shift of aqueous ions,  
8 are responsible for particle triboelectric charging, contact or triboelectric charging is  
9 the primary mechanism (e.g. Harrison et al., 2016; Lacks and Sankaran, 2011; Zheng,  
10 2013). In previous model, however, the charge-to-mass ratios of the saltating particles  
11 are either assumed to be a constant value (e.g. Schmidt et al., 1998; Zhang et al., 2014;  
12 Zheng et al., 2003), or are not accounted for in the particle-particle midair collisions  
13 (e.g. Kok and Renno, 2008). In this study, by using DEM together with an asymmetric  
14 contact electrification model, we account for the particle-particle triboelectric  
15 charging during midair collisions in saltation. The DEM implemented by cell-based  
16 algorithms is effective to detect and evaluate most of the particle-particle midair  
17 collisional dynamics (Norouzi et al., 2016). Meanwhile, the charge transfer between  
18 colliding particles can be determined by Eqs. (25) and (26). Compared to the previous  
19 studies (e.g. Kok and Lacks, 2009), the main innovation of this model is that the  
20 comprehensive consideration of the particle collisional dynamics affecting particle  
21 charge transfer is involved. In summary, the present model is a particle-particle midair  
22 collision resolved model, and the predicted charge-to-mass ratio agrees well with the  
23 published measurement data (see Fig. 7c). These findings indicate that midair  
24 collisions in saltation are important, both in momentum and charge exchanges.

25 One limitation of our model is that the effects of turbulent fluctuations on particle  
26 charging and dynamics are not explicitly accounted for. In actual conditions, saltation  
27 is unsteady and inhomogeneous at small scales, and the wind flow is mathematically  
28 described by the continuity and Navier-Stokes equations. However, in many cases,  
29 wind flow is statistically steady and homogeneous over a typical timescale of 10 min

1 (Durán et al., 2011; Kok et al., 2012). For example, in the relatively stationary period in  
2 Fig.5, all long-period averaged statistics become independent of time. In this case, the  
3 governing equations of the wind flow can be reduced to a simple model described by  
4 equation Eq. (13). There is no doubt that 3-D turbulent fluctuations could affect  
5 particle charging and dynamics considerably (e.g. Cimorelli et al., 2013; Dupont et al.,  
6 2013). Further work is therefore needed to incorporate turbulence into the numerical  
7 model.

#### 8 9 **5.4. Implications for evaluating particle triboelectric charging in dust events**

10 It is generally accepted that E-field could considerably affect the lifting and  
11 transport of sand particles. As the findings of previous 1-D E-field models (e.g. Kok and  
12 Renno, 2008), the E-field has been proven to inhibit sand transport in our model, when  
13 considering the vertical component of the E-field alone. *It is worth noting that, unlike  
14 the natural 1-D E-field produced by the charged sand particles, the man-made 1-D E-  
15 field may enhance sand transport in pure saltation. For example, Rasmussen et al.  
16 (2009) found that sand mass flux in pure saltation is significantly enhanced when a  
17 downward-pointing external E-field (opposite to the direction of actual vertical E-field)  
18 with magnitude of  $270 \text{ kV m}^{-1}$  is applied.* In contrast to the 1-D E-field, our model  
19 further shows that the real 3-D E-field in dust storms enhances sand transport  
20 substantially, consistent with a recent measurement by Esposito et al. (2016). This 3-D  
21 E-field model may resolve the discrepancy between the 1-D E-field model in pure  
22 saltation (e.g. Kok and Renno, 2008) and the recent measurement in dust storms (i.e.  
23 Esposito et al., 2016). In addition, the saltation height has also been enhanced by 3-D  
24 E-field. Therefore, it is necessary to consider 3-D E-field in further studies.

25 However, a remaining critical challenge is still to simulate particle triboelectric  
26 charging in dust storms precisely. The driving atmospheric turbulent flows having a  
27 typical Reynolds number on the order of  $10^8$  cover a broad range of length and time  
28 scales, which needs huge computational cost to resolve (e.g. Shao, 2008). On the other  
29 hand, particle triboelectric charging is so sensitive to particle's collisional dynamics

1 that it needs to resolve each particle collisional dynamics (e.g. Hu et al., 2012; Lacks  
2 and Sankaran, 2011). To model the particle's collisional dynamics properly, the time  
3 steps of DEM are generally from  $10^{-7}$  to  $10^{-4}$  s (Norouzi et al., 2016). However, steady-  
4 state saltation motion often requires several seconds to several tens of seconds to  
5 reach the equilibrium state. In this study, when  $u_* = 0.5 \text{ m s}^{-1}$  and the computational  
6 domain is  $0.5 \times 0.1 \times 1.0 \text{ m}^3$ , the total number of saltating particles exceeds  $7 \times 10^4$  (Fig.  
7 S8 in the Supplement). Consequently, the triboelectric charging in saltation is currently  
8 very difficult to simulate, where a large number of polydisperse sand particles, the high  
9 Reynolds-number turbulent flow, and the inter-particle electrostatic forces are  
10 mutually coupled. In the present version of the model, we do not consider the particle-  
11 particle interactions such as particle agglomeration and fragmentation during particle  
12 collision or frictional contact, as well as the particle-turbulence interaction that is the  
13 effects of turbulent fluctuations on the triboelectric charging and dynamics of particles.  
14 Further studies require considerable effort to incorporate these interactions [into a](#)  
15 [tractable numerical model](#), especially turbulence, which is very important for large  
16 wind velocity.

17

## 18 **6. Conclusions**

19 Severe dust storms occurring in arid and semiarid regions threaten human lives  
20 and result in substantial economic damages. Intense E-field up to  $\sim 100 \text{ kV m}^{-1}$  does  
21 exist in dust storms and could strongly affect particle dynamics. In this study, we  
22 performed the field measurements of 3-D E-field in the sub-meter layer from 0.05 to  
23 0.7 m above the ground during dust storms by VREFM sensors. Meanwhile, by  
24 introducing the DEM and asymmetric charging mechanism into the saltation model,  
25 we numerically study the effects of 3-D E-field on saltation. Overall, our results show  
26 that: (1) measured 3-D E-field data roughly collapse on the 3-order polynomial curves  
27 when normalized, providing a simple representation of the 3-D E-field during dust  
28 storms for the first time; (2) the inclusion of 3-D E-field in saltation model may resolve  
29 the discrepancy between previous 1-D E-field model (e.g. Kok and Renno, 2008) and

1 measurements (Esposito et al., 2016) in the aspect of whether the E-field inhibits or  
2 enhances saltation; (3) midair collisions dramatically affect both momentum and  
3 charge exchanges between saltating particles; and (4) the model predicts that 3-D E-  
4 field enhances the total mass flux and saltation height significantly, suggesting that 3-  
5 D E-field should be considered in future models, especially for dust storms.

6 We have also performed discussions about various sensitive parameters such as  
7 the density of charged species, the coefficient of restitution, and the height-averaged  
8 time-varying mean of the 3-D E-field. These results significantly add new knowledge to  
9 the role of particle triboelectric charging in determining the transport and lifting of  
10 sand and dust particles. A great effort is further needed to understanding the  
11 interactions such as particle agglomeration and fragmentation, as well as the effects  
12 of the turbulence on the triboelectric charging and dynamics of particles.

13

#### 14 **Data availability**

15 The E-field data recorded in our field campaign are provided as a CSV file in the  
16 Supplement.

17

#### 18 **Author contribution**

19 H.Z. performed the field observations, numerical simulation, and data analyses as  
20 well as wrote the manuscript, which was guided and edited by Y.H.Z. All authors  
21 discussed the results and commented on the manuscript.

22

#### 23 **Competing interests**

24 The authors declare that they have no conflict of interest.

25

#### 26 **Acknowledgments**

27 We thank the editor and anonymous reviewers for their insightful comments that  
28 greatly improve the final manuscript. This work was supported by the National Natural  
29 Science Foundation of China (grant number 11802109), the Young Elite Scientists

1 Sponsorship Program by CAST (grant number 2017QNRC001), and the Fundamental  
2 Research Funds for the Central Universities (grant number lzujbky-2018-7).

#### 4 **References**

5 Ai, J., Chen, J. F., Rotter, J. M., and Ooi, J. Y.: Assessment of rolling resistance models in  
6 discrete element simulations, *Powder Technol.*, 206, 269–282,  
7 doi:10.1016/j.powtec.2010.09.030, 2011.

8 Anderson, R. S., and Hallet, B.: Sediment transport by wind: toward a general model,  
9 *Geol. Soc. Am. Bull.*, 97, 523–535, doi: 10.1130/0016-  
10 7606(1986)97<523:STBWTA>2.0.CO;2, 1986.

11 Anderson, R. S., and Haff, P. K.: Simulation of eolian saltation, *Science*, 241, 820–823,  
12 doi:10.1126/science.241.4867.820, 1988.

13 Anderson, R. S., and Haff, P. K.: Wind modification and bed response during saltation  
14 of sand in air, *Acta Mech.*, 1, 21–51, doi:10.1007/978-3-7091-6706-9\_2, 1991.

15 Bagnold, R.: *The Physics of Blown Sand and Desert Dunes*, Chapman & Hall, London,  
16 1941.

17 [Bendat, J. S., and Piersol, A. G.: \*Random data: analysis and measurement procedures\*,  
18 \*John Wiley & Sons, Hoboken, 2011.\*](#)

19 Bo, T. L., Zhang, H., and Zheng, X. J.: Charge-to-mass ratio of saltating particles in wind-  
20 blown sand, *Sci. Rep.*, 4, 5590, doi:10.1038/srep05590, 2014.

21 Bo, T. L., and Zheng, X. J.: A field observational study of electrification with in a dust  
22 storm in Minqin, China, *Aeolian Res.*, 8, 39–47, doi:10.1016/j.aeolia.2012.11.001,  
23 2013.

24 Brilliantov, N. V., Spahn, F., Hertzsch, J. M., and Poschel, T.: Model for collisions in  
25 granular gases, *Phys. Rev. E*, 53, 5382, doi:10.1103/PhysRevE.53.5382, 1996.

26 Carneiro, M. V., Araújo, N. A., Pähtz, T., and Herrmann, H. J.: Midair collisions enhance  
27 saltation, *Phys. Rev. Lett.*, 115, 058001, doi:10.1103/PhysRevLett.111.058001,  
28 2013.

29 Cheng, N. S.: Simplified settling velocity formula for sediment particle, *J. Hydraul. Eng.*,

1 123, 149–152, doi:10.1061/(ASCE)0733-9429(1997)123:2(149), 1997.

2 [Cimarelli, C., Alatorre-Ibargüengoitia, M. A., Kueppers, U., Scheu, B., and Dingwell, D.](#)

3 [B.: Experimental generation of volcanic lightning, \*Geology\*, 42, 79–82, doi:](#)

4 [10.1130/G34802.1, 2014.](#)

5 Daubechies, I. (1990). The wavelet transform, time-frequency localization and signal

6 analysis. *IEEE transactions on information theory*, 36(5), 961–1005.

7 Dupont, S., Bergametti, G., Marticorena, B., and Simoens, S.: Modeling saltation

8 intermittency, *J. Geophys. Res.-Atmos.*, 118, 7109–7128, doi:10.1002/jgrd.50528,

9 2013.

10 [Durán, O., Claudin, P., and Andreotti, B.: On aeolian transport: Grain-scale interactions,](#)

11 [dynamical mechanisms and scaling laws, \*Aeolian Res.\*, 3, 243 – 270, doi:](#)

12 [10.1016/j.aeolia.2011.07.006, 2011.](#)

13 Esposito, F., Molinaro, R., Popa, C.I., Molfese, C., Cozzolino, F., Marty, L., Taj-Eddine, K.,

14 Achille, G. D., Franzese, G., and Silvestro, S.: The role of the atmospheric electric

15 field in the dust lifting process, *Geophys. Res. Lett.*, 43, 5501–5508,

16 doi:10.1002/2016GL068463, 2016.

17 [Flandrin, P., Rilling, G., and Goncalves, P.: Empirical mode decomposition as a filter](#)

18 [bank, \*IEEE Signal Process. Lett.\*, 11, 112–114, doi: 10.1109/LSP.2003.821662,](#)

19 [2004.](#)

20 Grinsted, A., Moore, J. C., and Jevrejeva, S.: Application of the cross wavelet transform

21 and wavelet coherence to geophysical time series, *Nonlinear Proc. Geoph.*, 11,

22 561–566, doi: 10.5194/npg-11-561-2004, 2004.

23 Haff, P. K., and Anderson, R. S.: Grainscale simulations of loose sedimentary beds: the

24 example of grain-bed impacts in aeolian saltation, *Sedimentology*, 40, 175–198,

25 doi:10.1111/j.1365-3091.1993.tb01760.x, 1993.

26 Harrison, R. G., Barth, E., Esposito, F., Merrison, J., Montmessin, F., Aplin, K. L., Borlina,

27 C., Berthelie, J. J., Dprez, G., and Farrell, W. M.: Applications of electrified dust

28 and dust devil electrostatics to martian atmospheric electricity, *Space Sci. Rev.*,

1 203, 299–345, doi:10.1007/s11214-016-0241-8, 2016.

2 Hu, W., Xie, L., and Zheng, X.: Contact charging of silica glass particles in a single  
3 collision, *Appl. Phys. Lett.*, 101, 114107, doi:10.1063/1.4752458, 2012.

4 Huang, H. J., Bo, T. L., and Zhang, R.: Exploration of splash function and lateral velocity  
5 based on three-dimensional mixed-size grain/bed collision. *Granul. Matter*, 19(4),  
6 73, doi: 10.1007/s10035-017-0759-9, 2017.

7 [Huang, N., Zhang, Y., and D'Adamo, R.: A model of the trajectories and midair collision  
8 probabilities of sand particles in a steady state saltation cloud, \*J. Geophys. Res.-  
9 Atmos.\*, 112, doi: 10.1029/2006JD007480, 2007.](#)

10 Huang, N. E., Shen, Z., Long, S. R., Wu, M. C., Shih, H. H., Zheng, Q., Yen, N. C., Tung, C.  
11 C., and Liu, H. H.: The empirical mode decomposition and the Hilbert spectrum  
12 for nonlinear and non-stationary time series analysis, *Proc. R. Soc. A-Math. Phys.  
13 Eng. Sci.*, 454, 903–995, doi:10.1098/rspa.1998.0193, 1998.

14 Huang, N. E., and Wu, Z.: A review on Hilbert-Huang transform: Method and its  
15 applications to geophysical studies, *Rev. Geophys.*, 46, RG2006,  
16 doi:10.1029/2007RG000228, 2008.

17 [Hutchins, N., Chauhan, K., Marusic, I., Monty, J., and Klewicki, J.: Towards reconciling  
18 the large-scale structure of turbulent boundary layers in the atmosphere and  
19 laboratory, \*Boundary-Layer Meteorol.\*, 145, 273–306, doi: 10.1007/s10546-012-  
20 9735-4, 2012.](#)

21 Jackson, T. L., and Farrell, W. M.: Electrostatic fields in dust devils: an analog to Mars,  
22 *IEEE Trans. Geosci. Remote Sensing*, 44, 2942–2949,  
23 doi:10.1109/TGRS.2006.875785, 2006.

24 Kamra, A. K.: Measurements of the electrical properties of dust storms, *J. Geophys.  
25 Res.*, 77, 5856–5869, doi:10.1029/JC077i030p05856, 1972.

26 Kawamura, R.: Study on sand movement by wind, Technical Report, Institute of Science  
27 and Technology, University of Tokyo, 5, 95–112, 1951.

28 [Kunkel, G. J., and Marusic, I.: Study of the near-wall-turbulent region of the high-  
29 Reynolds-number boundary layer using an atmospheric flow, \*J. Fluid Mech.\*, 548,](#)



1            [375–402, doi: 10.1017/S0022112005007780, 2006.](#)

2    Kok, J. F., and Lacks, D. J.: Electrification of granular systems of identical insulators, *Phys.*  
3            *Rev. E*, 79, 051304, doi:10.1103/PhysRevE.79.051304, 2009.

4    Kok, J. F., Parteli, E. J., Michaels, T. I., and Karam, D. B.: The physics of wind-blown sand  
5            and dust, *Rep. Prog. Phys.*, 75, 106901, doi:10.1088/0034-4885/75/10/106901,  
6            2012.

7    Kok, J. F., and Renno, N. O.: Electrostatics in wind-blown sand, *Phys. Rev. Lett.*, 100,  
8            014501, doi:10.1103/PhysRevLett.100.014501, 2008.

9    Kok, J. F., and Renno, N. O.: A comprehensive numerical model of steady state saltation  
10            (COMSALT), *J. Geophys. Res.-Atmos.*, 114, doi:10.1029/2009JD011702, 2009.

11    Lacks, D. J., and Sankaran, R. M.: Contact electrification of insulating materials, *J. Phys.*  
12            *D-Appl. Phys.*, 44, 453001, doi:10.1088/0022-3727/44/45/453001, 2011.

13    Lettau, K., and Lettau, H. H.: Experimental and micro-meteorological field studies of  
14            dune migration, in Lettau, K., and Lettau, H. H., eds., *Exploring the World’s Driest*  
15            *Climate*, Institute for Environmental Studies, University of Wisconsin Madison,  
16            110–147, 1978.

17    Loth, E.: Lift of a spherical particle subject to vorticity and/or spin, *AIAA J.*, 46, 801–  
18            809, doi:10.2514/1.29159, 2008.

19    Marticorena, B., and Bergametti, G.: Modeling the atmospheric dust cycle: 1. design  
20            of a soil-derived dust emission scheme, *J. Geophys. Res.-Atmos.*, 100, 16415–  
21            16430, doi:10.1029/95JD00690, 1995.

22    Martin, R. L., and Kok, J. F.: Wind-invariant saltation heights imply linear scaling of  
23            aeolian saltation flux with shear stress, *Sci. Adv.*, 3, e1602569, doi:  
24            10.1126/sciadv.1602569, 2017.

25    [Merrison, J. P.: Sand transport, erosion and granular electrification, \*Aeolian Res.\*, 4, 1–](#)  
26            [16, doi: 10.1016/j.aeolia.2011.12.003, 2012.](#)

27    Minier, J. P.: Statistical descriptions of polydisperse turbulent two-phase flows, *Phys.*  
28            *Rep.*, 665, 1–122, doi:10.1016/j.physrep.2016.10.007, 2016.

29    Norouzi, H. R., Zarghami, R., Sotudeh-Gharebagh, R., and Mostoufi, N.: Coupled CFD-

1 DEM modeling: formulation, implementation and application to multiphase flows,  
2 John Wiley & Sons, Chichester, 2016.

3 Owen, P. R.: Saltation of uniform grains in air, *J. Fluid Mech.*, 20, 225–242,  
4 doi:10.1017/S0022112064001173, 1964.

5 Pähz, T., Omeradžić, A., Carneiro, M. V., Araújo, N. A., and Herrmann, H. J.: Discrete  
6 Element Method simulations of the saturation of aeolian sand transport, *Geophys.*  
7 *Res. Lett.*, 42, 2063–2070, doi:10.1002/2014GL062945, 2015.

8 Percival, D. B., Walden, A. T.: *Wavelet methods for time series analysis*, Cambridge, UK,  
9 Cambridge UP, 2000.

10 Rasmussen, K. R., Kok, J. F., and Merrison, J. P.: Enhancement in wind-driven sand  
11 transport by electric fields, *Planet Space Sci.*, 57, 804–808,  
12 doi:10.1016/j.pss.2009.03.001, 2009.

13 [Di Renzo, M., and Urzay, J.: Aerodynamic generation of electric fields in turbulence](#)  
14 [laden with charged inertial particles, \*Nat. Commun.\*, 9, 1 – 11, doi:](#)  
15 [10.1038/s41467-018-03958-7, 2018.](#)

16 Rice, M. A., Willetts, B. B., and McEwan, I. K.: Observations of collisions of saltating  
17 grains with a granular bed from high-speed cine-film, *Sedimentology*, 43, 21–31,  
18 doi:10.1111/j.1365-3091.1996.tb01456.x, 1996.

19 Rudge, W. A. D.: Atmospheric electrification during South African dust storms, *Nature*,  
20 91, 31–32, doi:10.1038/091031a0, 1913.

21 Schmidt, D. S., Schmidt, R. A., and Dent, J. D.: Electrostatic force on saltating sand, *J.*  
22 *Geophys. Res.-Atmos.*, 103, 8997–9001, doi:10.1029/98JD00278, 1998.

23 Shao, Y. P.: *Physics and Modelling of Wind Erosion*, Springer Science & Business Media,  
24 Heidelberg, 2008.

25 Sherman, D. J., and Li, B.: Predicting aeolian sand transport rates: A reevaluation of  
26 models, *Aeolian Res.*, 3, 371–378, doi: 10.1016/j.aeolia.2011.06.002, 2012.

27 Silbert, L. E., Ertaş, D., Grest, G. S., Halsey, T. C., Levine, D., and Plimpton, S. J.: Granular  
28 flow down an inclined plane: Bagnold scaling and rheology, *Phys. Rev. E*, 64,  
29 051302, doi:10.1103/PhysRevE.64.051302, 2001.

- 1 Sørensen, M.: On the rate of aeolian transport, *Geomorphology*, 59, 53–62,  
2 doi:10.1016/j.geomorph.2003.09.005, 2004.
- 3 Sørensen, M., and McEwan, I.: On the effect of mid-air collisions on aeolian saltation,  
4 *Sedimentology*, 43, 65–76, doi: 10.1111/j.1365-3091.1996.tb01460.x, 1996.
- 5 Su, Y., Huang, G., and Xu, Y. L.: Derivation of time-varying mean for non-stationary  
6 downburst winds, *J. Wind Eng. Ind. Aerod.*, 141, 39 – 48, doi:  
7 10.1016/j.jweia.2015.02.008, 2015.
- 8 Tuley, R., Danby, M., Shrimpton, J., and Palmer, M.: On the optimal numerical time  
9 integration for lagrangian dem within implicit flow solvers, *Comput. Chem. Eng.*,  
10 34, 886–899, doi:10.1016/j.compchemeng.2009.10.003, 2010.
- 11 White, B. R., and Schulz, J. C.: Magnus effect in saltation, *J. Fluid Mech.*, 81, 497–512,  
12 doi:10.1017/S0022112077002183, 1977.
- 13 Williams, E., Nathou, N., Hicks, E., Pontikis, C., Russell, B., Miller, M., and Bartholomew,  
14 M. J.: The electrification of dust-lofting gust fronts (haboobs) in the sahel, *Atmos.*  
15 *Res.*, 91, 292–298, doi:10.1016/j.atmosres.2008.05.017, 2009.
- 16 Wu, Z., and Huang, N. E.: Ensemble empirical mode decomposition: a noise-assisted  
17 data analysis method, *Adv. Adaptive Data Anal.*, 1, 1–41, doi:  
18 10.1142/S1793536909000047, 2009.
- 19 Wu, Z., Huang, N. E., Wallace, J. M., Smoliak, B. V., and Chen, X.: On the time-varying  
20 trend in global-mean surface temperature, *Clim. Dyn.*, 37, 759–773,  
21 doi:10.1007/s00382-011-1128-8, 2011.
- 22 Xie, L., Ling, Y., and Zheng, X.: Laboratory measurement of saltating sand particles’  
23 angular velocities and simulation of its effect on saltation trajectory, *J. Geophys.*  
24 *Res.-Atmos.*, 112, D12116, doi:10.1029/2006JD008254, 2007.
- 25 Yair, Y., Katz, S., Yaniv, R., Ziv, B., and Price, C.: An electrified dust storm over the Negev  
26 desert, Israel, *Atmos. Res.*, 181, 63–71, doi:10.1016/j.atmosres.2016.06.011,  
27 2016.
- 28 Zhang, H., Bo, T. L., and Zheng, X.: Evaluation of the electrical properties of dust storms  
29 by multi-parameter observations and theoretical calculations, *Earth Planet. Sci.*

1 Lett., 461, 141–150, doi:10.1016/j.epsl.2017.01.001, 2017.

2 Zhang, H., and Zheng, X.: Quantifying the large-scale electrification equilibrium effects  
3 in dust storms using field observations at Qingtu Lake Observatory, *Atmos. Chem.*  
4 *Phys.*, 18, 17087–17097, doi:10.5194/acp-18-17087-2018, 2018.

5 Zhang, H., Zheng, X. J., and Bo, T. L.: Electrification of saltating particles in wind-blown  
6 sand: Experiment and theory, *J. Geophys. Res.-Atmos.*, 118, 12086 – 12093.  
7 doi:10.1002/532 2013JD020239, 2013.

8 Zhang, H., Zheng, X. J., and Bo, T. L.: Electric fields in unsteady wind-blown sand, *Eur.*  
9 *Phys. J. E*, 37, 13, doi:10.1140/epje/i2014-14013-6, 2014.

10 Zheng, X. J.: Electrification of wind-blown sand: recent advances and key issues, *Eur.*  
11 *Phys. J. E*, 36, 138, doi:10.1140/epje/i2013-13138-4, 2013.

12 Zheng, X. J., Huang, N., and Zhou, Y. H.: Laboratory measurement of electrification of  
13 wind-blown sands and simulation of its effect on sand saltation movement, *J.*  
14 *Geophys. Res.-Atmos.*, 108, doi:10.1029/2002JD002572, 2003.

15

1 **Table 1.** Description of all variables used in this study.

Symbols	Physical meaning	Units
$a_{0,i}, a_{1,i}, a_{2,i}, a_{3,i}$	fitting coefficients in Eq. (8)	1
$C_d$	drag coefficient	1
$C_m$	normalized spin lift coefficient in Magnus force formula	1
$d_p$	particle diameter	m
$d_i, d_j$	diameters of particle $i$ and $j$	m
$d_m$	mean diameter of particle sample in the numerical model	m
$D_{imp}, D_{ej}^k$	diameter of the impact and ejected particles	m
$e_n$	coefficient of restitution of particles	1
$E$	a time series of measured E-field	kV m <sup>-1</sup>
$\bar{E}$	time-varying mean values of $E(t)$	kV m <sup>-1</sup>
$\langle \bar{E}_i \rangle$	height-averaged time-varying mean values of $E(t)$	kV m <sup>-1</sup>
$E_i^*(z^*)$	dimensionless E-field of component $i$	1
$E_1, E_2, E_3$	streamwise, spanwise, and vertical components of E-field	kV m <sup>-1</sup>
$\vec{F}_i^d, \vec{F}_i^m$	drag force and Magnus force acting on particle $i$	N
$\vec{F}_{ij}^d, \vec{F}_{ij}^t$	the normal and tangential collisional forces	N
$g=9.81$	gravitational acceleration	m s <sup>-2</sup>
$G$	shear modulus of particles	Pa
$G^*$	equivalent shear modulus between two contacting particles	Pa
$I_i$	moment of inertia of particle $i$	kg m <sup>2</sup>
$L_x, L_y$	streamwise and spanwise width of the computational domain	m
$m^*$	equivalent particle mass between two contacting particles	kg
$m_{p,i}$	mass of particle $i$	kg
$m_c$	mean particle mass concentration	kg m <sup>-3</sup>
$\vec{M}_i^{w-p}, \vec{M}_{ij}^c, \vec{M}_{ij}^r$	torque due to the wind, the torque due to the tangential component of the particle collisional forces, and the rolling resistance torque	N·m
$\vec{n}_{ij}$	unit vector in the direction from the center of particle $i$ point toward the center of particle $j$	-
$N$	number of the decomposition levels of DWT and EEMD	1
$N_e$	number of white noise series added to the original E-field series	1
$N_k$	number of ejected particles from the $k$ -th particle bin	1
$p_k$	mass fraction of the $k$ -th particle bin	1
$P_{reb}$	rebouncing probability of a saltating particle colliding with the sand bed	1
$q, Q$	mass flux and total mass flux defined in Eq. (26)	kg m <sup>-2</sup> s <sup>-1</sup> , Kg m <sup>-1</sup> s <sup>-1</sup>
$R^*$	equivalent particle radius between two contacting particles	m
$Re_p$	particle Reynolds number	1
$S_i, S_j$	contact area of particle $i$ and $j$	m <sup>2</sup>
$\vec{u}_r$	particle-to-wind relative velocity	m s <sup>-1</sup>
$u_m$	mean streamwise wind speed	m s <sup>-1</sup>
$u_*$	friction velocity	m s <sup>-1</sup>

**Table 1.** Continued.

<b>Symbols</b>	<b>Physical meaning</b>	<b>Units</b>
$\vec{u}_{p,i}$	velocity of particle $i$	$\text{m s}^{-1}$
$u_{p,i}, w_{p,i}$	streamwise and vertical components of particle velocity	$\text{m s}^{-1}$
$\langle u_p \rangle$	mean particle horizontal speed	$\text{m s}^{-1}$
$v_{imp}$	impact speed of the saltating particle	$\text{m s}^{-1}$
$\vec{v}_{ij}, \vec{v}_{ij}^n, \vec{v}_{ij}^t$	relative velocity between particle $i$ and $j$ at the contact point, and its normal and tangential components	$\text{m s}^{-1}$
$\vec{x}_i, \vec{x}_j$	position vectors of particle $i$ and $j$	$\text{m}$
$Y=10^8$	Young's modulus of particles	$\text{Pa}$
$Y^*$	equivalent Young's modulus between two contacting particles	$\text{Pa}$
$z, z^*$	height above the ground and dimensionless height	$\text{m}, 1$
$z_0$	the aerodynamic roughness	$\text{m}$
$z_{salt}$	saltation height	$\text{m}$
$\beta$	damping coefficient of collisional forces	$1$
$\gamma_s=0.5, \gamma_r=0.1$	coefficients of static and rolling friction	$1$
$\zeta_{p,i}$	charge-to-mass ratio of particle $i$	$\text{C kg}^{-1}$
$\eta_n$	residual of EEMD or EMD	-
$\theta, \varphi$	rebouncing angles of particles	$^\circ$
$\kappa \approx 0.41$	von Kármán constant	$1$
$\tau_p$	particle momentum flux	$\text{Pa}$
$\vec{\omega}_{p,i}$	angular velocity of the particle $i$	$\text{rad s}^{-1}$
$\delta_n, \delta_t$	normal and tangential overlap between two contacting particles	$\text{m}$
$\mu=1.8 \times 10^{-5}$	dynamic viscosity of the air	$\text{Pa}\cdot\text{s}$
$\nu=0.3$	Poisson's ratio of particles	$1$
$\xi_i$	EEMD component or IMF of EMD	-
$\rho_a=1.174$	air density	$\text{kg m}^{-3}$
$\rho_p=2650$	particle mass density	$\text{kg m}^{-3}$
$\rho_c$	space charge density	$\text{C m}^{-3}$
$\rho_h^i, \rho_h^j$	density of the electrons trapped in the high energy states on the surface of particle $i$ and $j$	$\text{m}^{-2}$
$\sigma$	surface charge density	$\text{C m}^{-2}$
$\sigma_p$	geometric standard deviation of particle sample in the numerical model	$1$
$\chi_N$	the $i$ -th level wavelet detail component	-
$\psi_i$	the $N$ -th level wavelet approximation component	-
$\Delta q_{ij}$	net increment of the charge of particle $i$ after colliding with particle $j$	$\text{C}$
$\Delta z$	vertical grid size	$\text{m}$

1

2

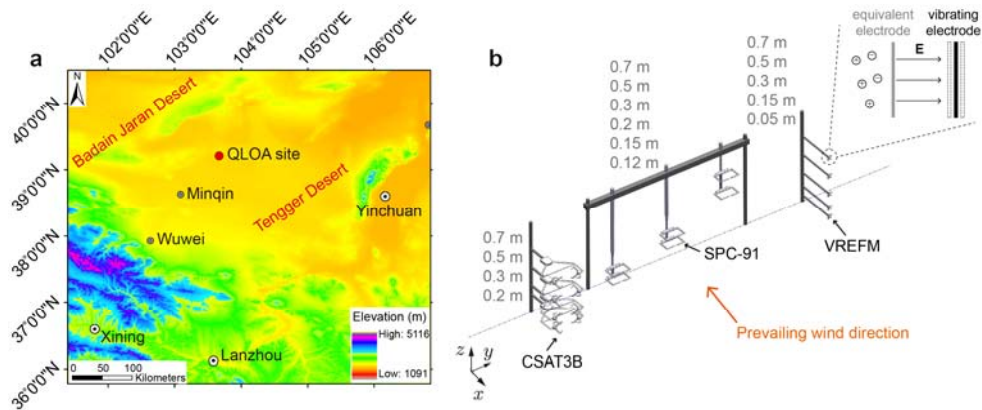
1 **Table 2.** Fitting coefficients of the 3-order polynomial curves in Fig. 5.

Components	$a_{0,i}$	$a_{1,i}$	$a_{2,i}$	$a_{3,i}$	$R^2$
$i = 1$	-2.17	4.02	-2.24	0.31	0.97
$i = 2$	-0.71	2.06	-1.49	0.23	0.80
$i = 3$	0.55	-1.41	1.24	-0.21	0.67

2

3

1



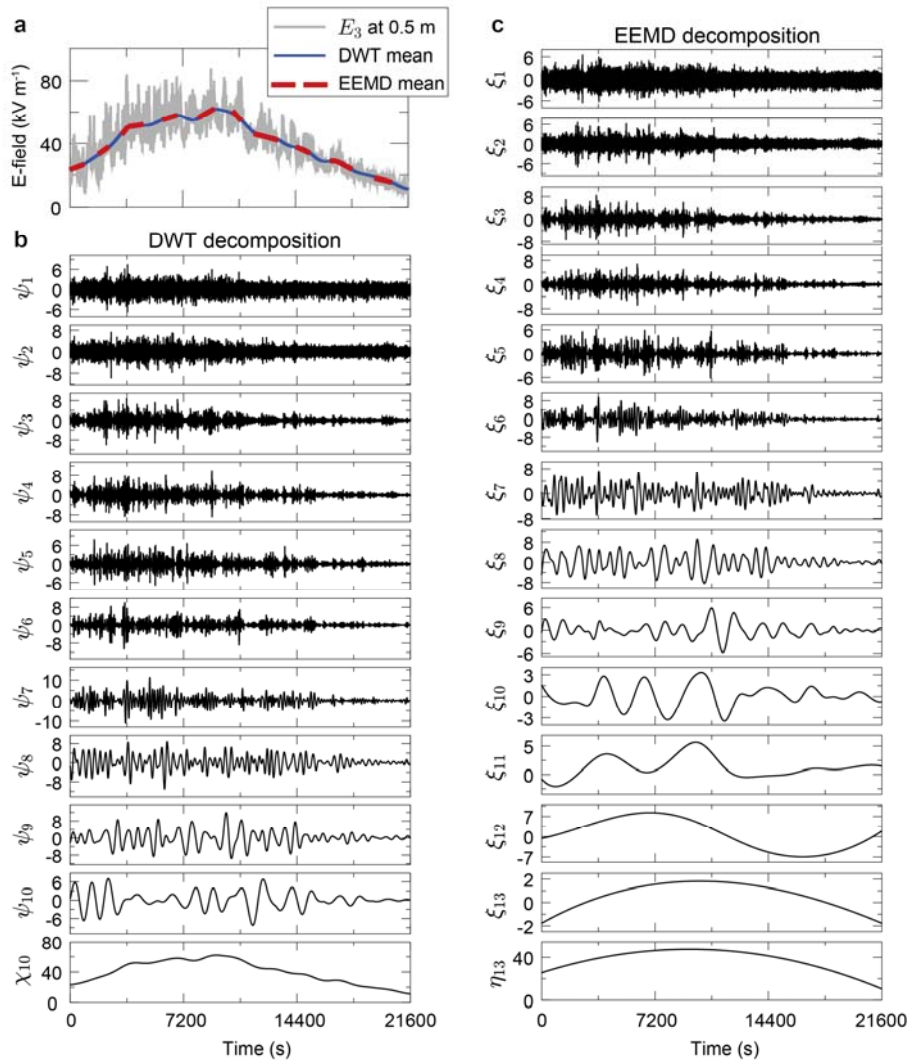
2

3 **Figure 1.** Map of the QLOA site and the layout of all instruments. (a) The QLOA site is  
4 located between the Badain Jaran Desert and the Tengger Desert, approximately 90  
5 km northeast of Minqin, Gansu, China. (b) Four CSAT3B sensors were mounted at 0.2-  
6 0.7 m height, respectively; six SPC-91 sensors were mounted at 0.12-0.7 m height,  
7 respectively; total fifteen VREFM sensors were mounted to measure the 3-D E-field at  
8 0.05-0.7 m height, respectively (that is, at each measurement point, three VREFM  
9 sensors are mutually perpendicular). The CSAT3B, SPC-91, and VREFM sensors were  
10 distributed along a straight line parallel to the  $y$  axis, and the prevailing wind  
11 direction in the QLOA site is parallel to the  $x$  axis. [The inset shows the working  
12 principle of the VREFM, where the charged particles and the vibrating electrode forms  
13 a dynamic capacity.](#)

14



1

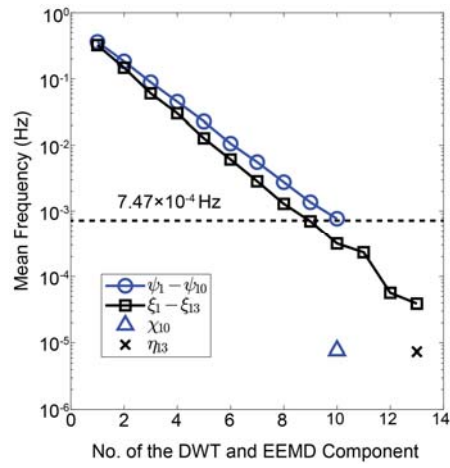


2

3 **Figure 2.** The resulting DWT and EEMD components from a measured vertical E-field  
 4 component  $E_3$  at 0.5 m height, with a total of  $N_d=21600$  data points. (a) shows the  
 5 original E-field time series (gray line), as well as the time-varying mean obtained by  
 6 DWT (blue line) and EEMD (red dashed line). (b) shows the detailed components  $\psi_1$ -  
 7  $\psi_{10}$  and approximation component  $\chi_{10}$  of DWT. (c) shows the EEMD components  
 8  $\xi_1$ - $\xi_{13}$  and the residue  $\eta_{13}$ . In the EEMD,  $N$  is specified as  $\log_2(N_d) - 1$ , the  
 9 member of ensemble  $N_e$  is 100, and the added white noise in each ensemble  
 10 member has a standard deviation of 0.2. Times are shown relative to May 6, 2014 at  
 11 13:00:00 UTC+8.

12

1



2

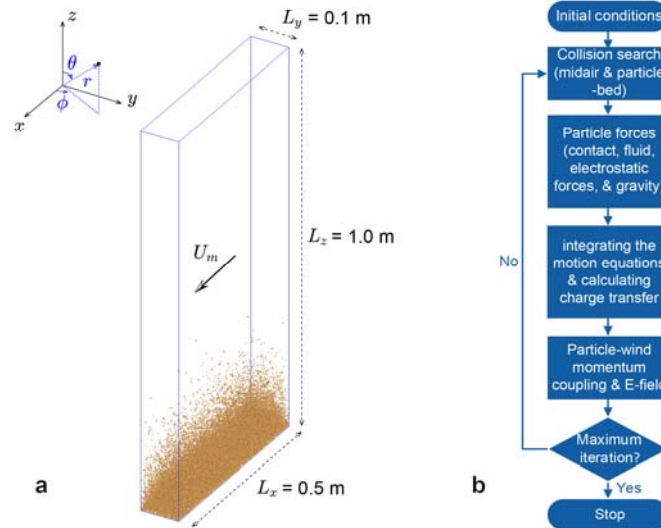
3 **Figure 3.** The Mean frequencies of DWT and EEMD components of  $E_3$  at 0.5 m height.

4 The dashed line around the components  $\psi_{10}$  and  $\xi_9$  corresponds to the frequency

5 of  $7.47 \times 10^{-4}$  Hz.

6

1

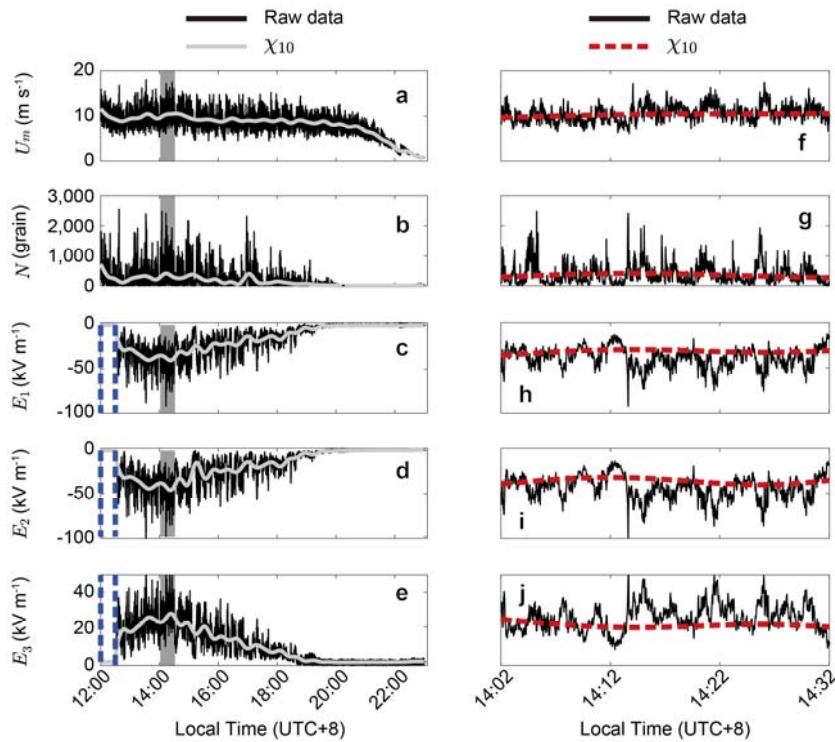


2

3 **Figure 4.** A schematic illustration of the DEM simulation of saltation and the numerical  
4 algorithm of the saltation model. (a) A 3-D view of the simulated wind-blown sand at  
5 the steady state, where the wind shear velocity  $u_* = 0.5 \text{ m s}^{-1}$ , average sand diameter  
6  $d_m = 228 \text{ }\mu\text{m}$ , and geometric standard deviation  $\sigma_p = \exp(0.3)$ . Both the Cartesian and  
7 spherical coordinates are shown in the inset. (b) This flowchart shows the scheme for  
8 simulating the saltation according to the following steps implementing the DEM with  
9 particle triboelectric charging: initial conditions, collision search, particle forces,  
10 integrating motion equations and calculating charge transfer, particle-wind  
11 momentum coupling and evaluating E-field, and finally repeating these execute steps  
12 until reaching the maximum iteration steps.

13

1

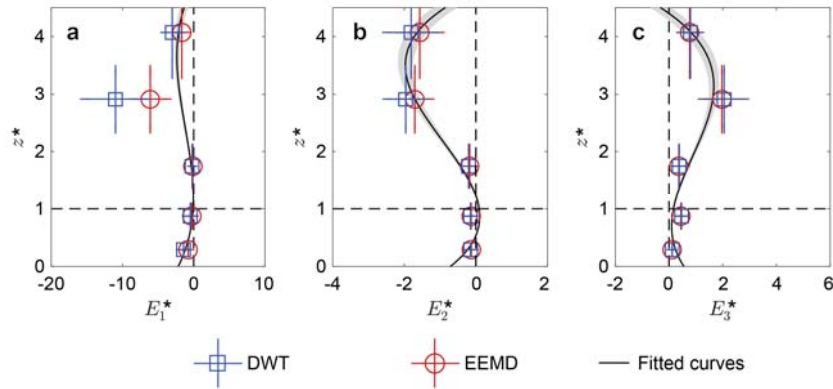


2

3 **Figure 5.** Measured results during a dust storm occurring on May 6, 2014, at the QLOA  
 4 site. (a)-(e): the measured time series of the streamwise wind speed,  $u_m$  at 0.7 m;  
 5 the number of saltating particle  $N$  at 0.15 m; streamwise E-field  $E_1$ , spanwise E-field  
 6  $E_2$ , and vertical E-field  $E_3$  at 0.7 m. Unfortunately, owing to the interruption of power  
 7 supply, the 3-D E-field data have not been recorded before  $\sim 12:30$ , as represented by  
 8 a dashed box in the last three panels (from top to bottom). The shaded area denotes  
 9 the relatively stationary period of the observed dust storm, because during this period  
 10 the time-varying means of all quantities (i.e.  $\chi_{10}$ ) do not vary notably as time varies  
 11 (Bendat and Piersol, 2011), as shown in (f)-(j).

12

1



2

3 **Figure 6.** Vertical profiles of the normalized 3-D E-field. Subgraphs (a)-(c), in turn,  
4 correspond to the vertical profiles of  $E_1^*$ ,  $E_2^*$ , and  $E_3^*$  of the observed dust storm.

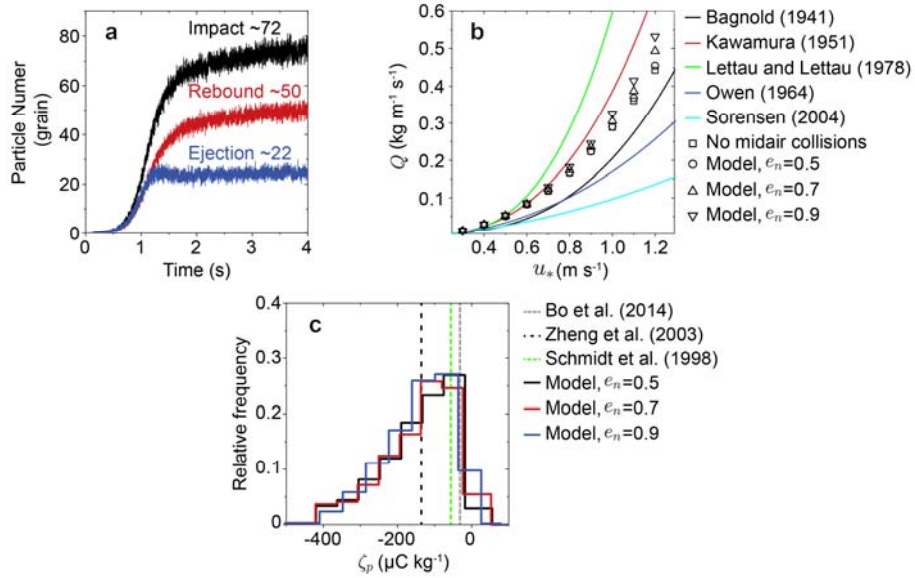
5 Squares and circles denote the DWT mean and EEMD mean values of the normalized  
6 E-field data, respectively. Error bars are standard deviations. Lines denote robust linear

7 least-squares fitting of the normalized E-field data obtained by DWT and EEMD  
8 method using 3-order polynomials (with  $R^2$  of 0.97, 0.80, and 0.67, respectively),

9 where the shaded areas denote 95% confidence bounds.

10

1



2

3 **Figure 7.** Verification of the steady-state numerical model in the case of pure saltation.

4 That is, only vertical E-field needs to be considered, which is produced by the charged

5 saltating particles. (a) The number of the impacting, rebounding, and ejected particles

6 within each time period of  $10^{-4}$  s, where  $u_* = 0.5$  m s<sup>-1</sup>,  $d_m = 228$  μm, and  $\sigma_p = \exp(0.3)$ .

7 (b) Comparison of the simulated total mass flux with the most commonly-used

8 semiempirical saltation mass flux equations (Bagnold, 1941; Kawamura, 1951; Lettau

9 and Lettau, 1978; Owen, 1964; Sørensen, 2004), where  $d_m = 228$  μm, and  $\sigma_p = \exp$

10 (0.3). (c) Comparison of the simulated charge-to-mass ratio distribution in the range

11 of 0.07-0.09 m height with the measured mean charge-to-mass ratio, in the range of

12 0.06-0.1 m height (Zheng et al., 2003), at 0.05 m height (Schmidt et al., 1998) and 0.08

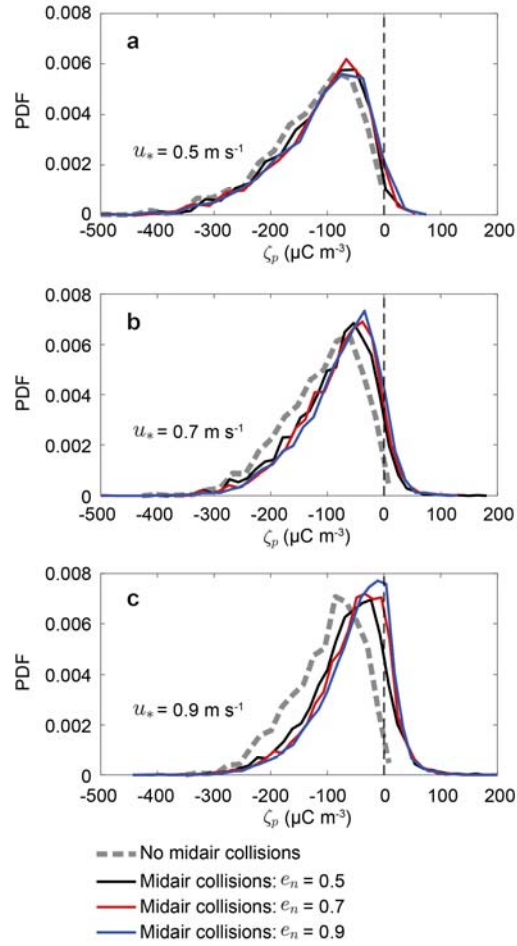
13 m height (Bo et al., 2014). Here,  $\rho_h^0 = 6 \times 10^{15}$  m<sup>-2</sup> is determined by calibrating the model

14 with measurements;  $u_* = 0.35$  m s<sup>-1</sup>,  $d_m = 203$  μm, and  $\sigma_p = \exp(0.33)$  are estimated

15 from (Zheng et al., 2003).

16

1

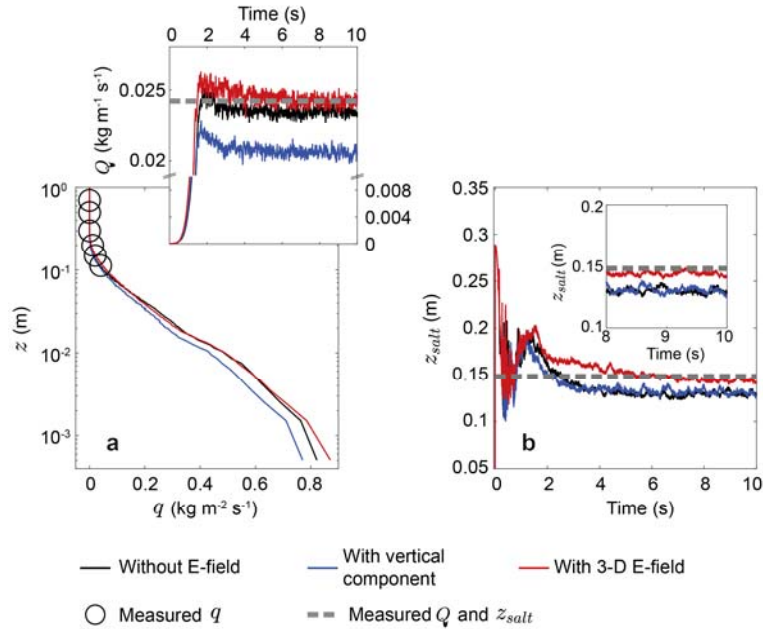


2

3 **Figure 8.** Effects of midair collisions on the probability density function (PDF) of charge-  
4 to-mass ratio of saltating particles for various wind velocities (a)  $u_* = 0.5 \text{ m s}^{-1}$ , (b)  
5  $u_* = 0.7 \text{ m s}^{-1}$ , and (c)  $u_* = 0.9 \text{ m s}^{-1}$ , where  $d_m = 203 \text{ }\mu\text{m}$ ,  $\sigma_p = \exp(0.33)$ , and  $\rho_h^0 = 6 \times 10^{15}$   
6  $\text{m}^{-2}$ .

7

1



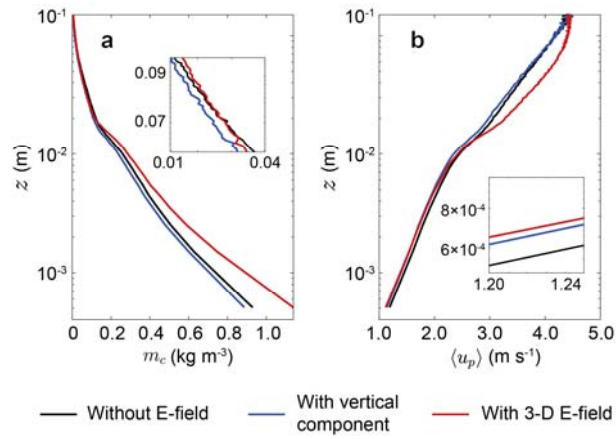
2

3 **Figure 9.** Comparison of the simulated mass flux  $q$  and total mass flux  $Q$  (a) and  
 4 saltation height  $z_{salt}$  (b) with our measurements in the relatively stationary period of  
 5 the observed dust storm (shaded areas in Fig. 4 and Fig. S3 in the Supplement), where  
 6  $u_* = 0.37 \text{ m s}^{-1}$ ,  $d_m = 200 \text{ }\mu\text{m}$ ,  $\sigma_p = \exp(0.42)$ ,  $\rho_h^0 = 6 \times 10^{15} \text{ m}^{-2}$ , and  $e_n = 0.7$ . (a) Circles  
 7 are the measured mean mass flux, dashed line denotes the estimated mean total mass  
 8 flux, and lines denote the simulated results. (b) Dashed lines denote the estimated  
 9 saltation height based on our measurements and lines denote simulated results. **Inset**  
 10 **shows the same data from 8 to 10 s.** The uncertainty analysis of the measured or  
 11 estimated results can be found in Text S1 in the Supplement.

12



1

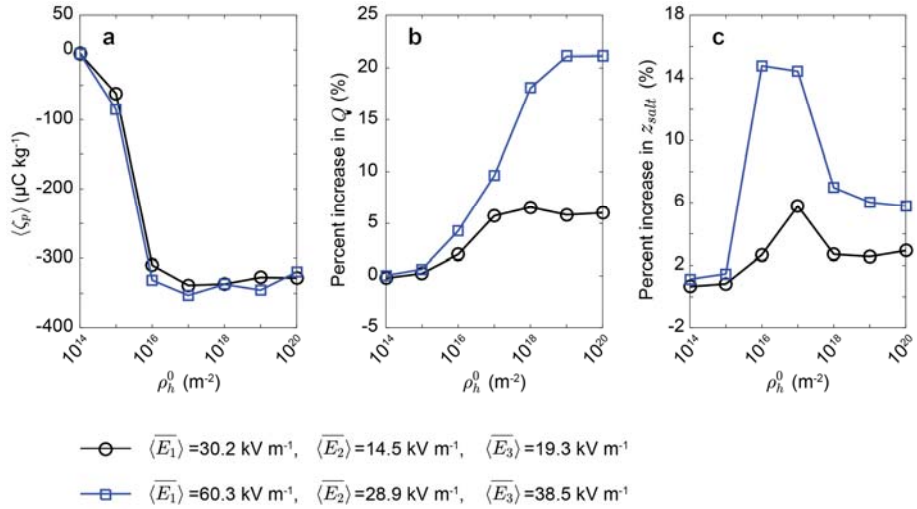


2

3 **Figure 10.** Vertical profiles of the particle mass concentration  $m_c$  and mean particle  
4 horizontal speed  $\langle u_p \rangle$  for different cases, where  $\langle u_p \rangle$  is calculated as the arithmetic  
5 mean of particle horizontal speed located in the range of  $[z, z + \Delta z]$ . Insets show the  
6 same data and emphasize the local information. In these cases  $u_* = 0.37 \text{ m s}^{-1}$ ,  
7  $d_m = 200 \text{ } \mu\text{m}$ ,  $\sigma_p = \exp(0.42)$ ,  $\rho_h^0 = 6 \times 10^{15} \text{ m}^{-2}$ , and  $e_n = 0.7$ .

8

1



2

3 **Figure 11.** Effects of the density of charged species  $\rho_h^0$  on saltation for two different  
 4 height-averaged time-varying mean levels (i.e.  $\langle \bar{E}_i \rangle$ ,  $i = 1,2,3$ ). (a) The mean charge-  
 5 to-mass ratio  $\langle \zeta_p \rangle$  (in the range from 0.07 to 0.09 m height) as a function of  $\rho_h^0$   
 6 ranging from  $10^{14}$  to  $10^{20} \text{ m}^{-2}$  (e.g. Kok and Lacks, 2009). (b) Percent increase in the  
 7 total mass flux  $Q$  as a function of  $\rho_h^0$ . (c) Percent increase in the saltation height  $z_{salt}$   
 8 as a function of  $\rho_h^0$ . The squares correspond to the height-averaged time-varying  
 9 mean in the **stationary** stage of the observed dust storm (shaded areas in Fig. S7 in the  
 10 Supplement). In these cases,  $e_n=0.7$ .